



Historical perspective

## Hardening of particle/oil/water suspensions due to capillary bridges: Experimental yield stress and theoretical interpretation



Krassimir D. Danov<sup>a</sup>, Mihail T. Georgiev<sup>a</sup>, Peter A. Kralchevsky<sup>a,\*</sup>, Gergana M. Radulova<sup>a</sup>, Theodor D. Gurkov<sup>a</sup>, Simeon D. Stoyanov<sup>b,c,d</sup>, Eddie G. Pelan<sup>b</sup>

<sup>a</sup> Department of Chemical & Pharmaceutical Engineering, Faculty of Chemistry and Pharmacy, Sofia University, Sofia 1164, Bulgaria

<sup>b</sup> Unilever Research & Development Vlaardingen, 3133AT Vlaardingen, The Netherlands

<sup>c</sup> Laboratory of Physical Chemistry and Colloid Science, Wageningen University, 6703, HB, Wageningen, The Netherlands

<sup>d</sup> Department of Mechanical Engineering, University College London, WC1E 7JE, UK

### ARTICLE INFO

Available online 21 November 2017

#### Keywords:

Capillary suspensions  
Capillary bridges  
Pendular state  
Yield stress  
Rheology of suspensions  
Wet granular materials

### ABSTRACT

Suspensions of colloid particles possess the remarkable property to solidify upon the addition of minimal amount of a second liquid that preferentially wets the particles. The hardening is due to the formation of capillary bridges (pendular rings), which connect the particles. Here, we review works on the mechanical properties of such suspensions and related works on the capillary-bridge force, and present new rheological data for the weakly studied concentration range 30–55 vol% particles. The mechanical strength of the solidified capillary suspensions, characterized by the yield stress  $Y$ , is measured at the elastic limit for various volume fractions of the particles and the preferentially wetting liquid. A quantitative theoretical model is developed, which relates  $Y$  with the maximum of the capillary-bridge force, projected on the shear plane. A semi-empirical expression for the mean number of capillary bridges per particle is proposed. The model agrees very well with the experimental data and gives a quantitative description of the yield stress, which increases with the rise of interfacial tension and with the volume fractions of particles and capillary bridges, but decreases with the rise of particle radius and contact angle. The quantitative description of capillary force is based on the exact theory and numerical calculation of the capillary bridge profile at various bridge volumes and contact angles. An analytical formula for  $Y$  is also derived. The comparison of the theoretical and experimental strain at the elastic limit reveals that the fluidization of the capillary suspension takes place only in a deformation zone of thickness up to several hundred particle diameters, which is adjacent to the rheometer's mobile plate. The reported experimental results refer to water-continuous suspension with hydrophobic particles and oily capillary bridges. The comparison of data for bridges from soybean oil and hexadecane surprisingly indicate that the yield strength is greater for the suspension with soybean oil despite its lower interfacial tension against water. The result can be explained with the different contact angles of the two oils in agreement with the theoretical predictions. The results could contribute for a better understanding, quantitative prediction and control of the mechanical properties of three-phase capillary suspensions solid/liquid/liquid.

© 2017 Elsevier B.V. All rights reserved.

### Contents

1. Introduction	81
1.1. Wet granular materials	81
1.2. Particle/oil/water suspensions	82
1.3. Number of capillary bridges per particle	83
2. Capillary bridges	83
2.1. Brief overview of preceding studies	83
2.2. Meniscus profile and capillary bridge force	84
2.3. The sequence of capillary bridges	85

\* Corresponding author.

E-mail address: [pk@lcpe.uni-sofia.bg](mailto:pk@lcpe.uni-sofia.bg) (P.A. Kralchevsky).

3. Experiments with particle/oil/water suspensions . . . . . 86  
 3.1. Experimental materials and procedures . . . . . 86  
 3.2. Experimental method . . . . . 86  
 3.3. Experimental results . . . . . 86  
 4. Theoretical description of the yield stress . . . . . 87  
 4.1. The elastic limit upon shear deformation – general approach . . . . . 87  
 4.2. Expression for the yield stress . . . . . 89  
 4.3. Exact numerical results . . . . . 90  
 5. Theoretical interpretation of rheological data . . . . . 92  
 5.1. The experimental yield stress . . . . . 92  
 5.2. Models of the deformation zone . . . . . 92  
 5.3. Theory vs. experiment and discussion . . . . . 93  
 6. Conclusions . . . . . 95  
 Acknowledgements . . . . . 95  
 Appendices A, B and C. Supplementary data . . . . . 95  
 References . . . . . 95

**1. Introduction**

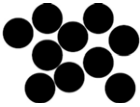




The present article is devoted to the investigation of mechanical properties of three-phase suspensions particles/oil/water. If the colloid particles have been initially dispersed in one of the two liquid phases, the addition of even minimal amount of the second liquid may lead to hardening of suspension. The solidified dispersion exhibits a high yield stress when subjected to mechanical deformation [1,2]. This effect can be used to control the flow behavior of suspensions that would otherwise require the addition of binding agents or other additives [3]. The solidification is due to the connection of particles by capillary bridges or menisci [1–9]. Spontaneous formation of capillary bridges upon agitation of the dispersion happens if the particles have affinity to the *inner liquid* (the liquid in the capillary bridges). Thus, the strongest hardening of dispersion takes place if hydrophilic particles are interconnected by water capillary bridges in oil, or hydrophobic particles are interconnected by oily capillary bridges in water. Our study is focused on the investigation of this effect; on the role of the

volume fractions of particles and inner liquid, and on the influence of interfacial tension and three-phase contact angle. The *yield stress* will be used to characterize the mechanical strength of the solidified suspension. Detailed theoretical model is proposed, which quantitatively describes the dependence of the yield stress on the system's physical parameters. A brief review of the accumulated knowledge on three-phase dispersions is following.

*1.1. Wet granular materials*

The traditional field of wet granular materials, corresponds to high particle volume fractions,  $\phi_p > 70\%$ , in the system solid/liquid/gas. The most famous examples are the wet sand and the sand castles. This field has been a subject of numerous experimental and theoretical studies; see Refs [10,11] for review. In the case of dry particle/gas dispersion (Table 1a), the interparticle cohesion (due mostly to van der Waals forces) is negligible in comparison with the cohesion due to capillary bridges.

**Table 1**  
 Changes in the morphology of wet granular materials (particles/liquid/gas) with the rise of volume fraction of the liquid phase [10].

Liquid content	State	Morphology	Physical description
(a) No	Dry		Weak cohesion between the particles.
(b) Small	Pendular		Capillary bridges (pendular rings) around contact points of neighboring particles; strong adhesion. The liquid is disperse phase; the gas is continuous phase.
(c) Middle	Funicular		Merging of capillary bridges. Both the liquid and gas phases are continuous – bicontinuous topology.
(d) High	Capillary		Gas-filled cavities remain between the particles, which are connected by the capillary menisci. The gas is disperse phase; the liquid is continuous phase.
(e) Maximal	Slurry		The particles are completely immersed in the liquid. The cohesion between them is weak.

Significant changes in the mechanical properties of the granular material happen in the presence of liquid that wets the particles, i.e. the solid/liquid/gas contact angle is  $\alpha < 90^\circ$ . If the liquid phase is present at a sufficiently low volume fraction (Table 1b), then it is a *disperse* phase, which forms concave capillary bridges (pendular rings) around the contact points of the neighboring particles [12]. The gas phase is the continuous phase. The respective state of the three-phase dispersion is termed the *pendular state*. The capillary bridge force, which connects the particles, causes solidification of the granular material [10].

With the increase of the volume fraction of liquid, the capillary bridges between the particles begin to overlap, so that the liquid phase is transformed into a second continuous phase. Thus, the dispersion undergoes a transition from the pendular state to the so called *funicular state* (Table 1c). In this state, the “flooded” three-phase dispersion is *bicontinuous* and mechanically softer than in the pendular state.

At higher liquid volume fractions, the gaseous phase becomes a *disperse* phase. It occupies cavities between the solid particles. Such a cavity can be considered as a gas bubble of irregular shape with several particles attached to its surface. Thus, the capillary menisci connect the particles and give rise to hardening of the three-phase dispersion. This is the so called *capillary state* of suspension (Table 1d). Finally, if all particles in the dispersion are completely wet by the liquid phase, the dispersion is transformed into *slurry* (Table 1e).

## 1.2. Particle/oil/water suspensions

The above classification can be extended to dispersions, in which the gas phase is exchanged with a second liquid phase. If the liquid 1 wets the particles significantly better than the liquid 2, the diagram in Table 1 will be applicable again, but with “liquid 1” and “liquid 2” instead of “liquid” and “gas”. Most frequently, the two liquids are oil (liquid hydrocarbon) and water.

Such three-phase solid/liquid/liquid systems, called also capillary suspensions, have been a subject of intensive studies in the last decade in the works by Koos, Willenbacher, and other researchers [1–3,6–9,13–15]. The capillary suspensions could find various applications, such as the preparation of novel food products [16,17]; slurries for printable electronics or generation of energy [18–21]; improved polymer blends [22–24]; precursors for glass or ceramic filters of high porosity [25–27], and thermal interfacial materials [28]. Semiempirical expressions for the yield stress in capillary suspensions have been proposed in Refs [4,9].

As already mentioned, in the traditional field of wet granular materials the particle volume fraction is high, about that at close packing of monodisperse spheres,  $\phi_p \approx 74\%$ . On the other hand, hardening (gelation) of three-phase dispersion can be observed also at significantly lower particle volume fractions,  $10\% < \phi_p < 25\%$  [1,6]. In this case, the hardening is due to the formation of particle networks, which span the whole volume of the dispersion. Large cavities are present in the formed network structure because of the relatively low particle volume fraction; see Refs [6,29].

In the ideal case of monodisperse spherical particles, the lowest particle volume fraction, at which one can fill the space with a regular lattice from particles that *touch each other* (no voids), is  $\phi_p \approx 34\%$ . The last value corresponds to a lattice of diamond type where each particle in the capillary suspension has four neighbors, which are connected by pendular rings (in the pendular state). For  $\phi_p < 34\%$ , the appearance of cavities (voids bigger than the particles) is unavoidable. In view of that, we could classify the capillary suspensions as *closely packed*, with  $\phi_p \approx 74\%$ ; *uniform* (without cavities), with  $34\% < \phi_p < 74\%$  (with coordination number  $4 \leq n \leq 12$ ; see Section 1.3), and *nonuniform* (with cavities) for  $\phi_p < 34\%$ ; see Fig. 1. The boundary values 34% and 74% are tentative, because with a greater number of closest neighbors ( $n > 4$ ) one could have cavities even for  $\phi_p > 34\%$ , whereas with polydisperse particles the close packing could take place for  $\phi_p > 74\%$ .

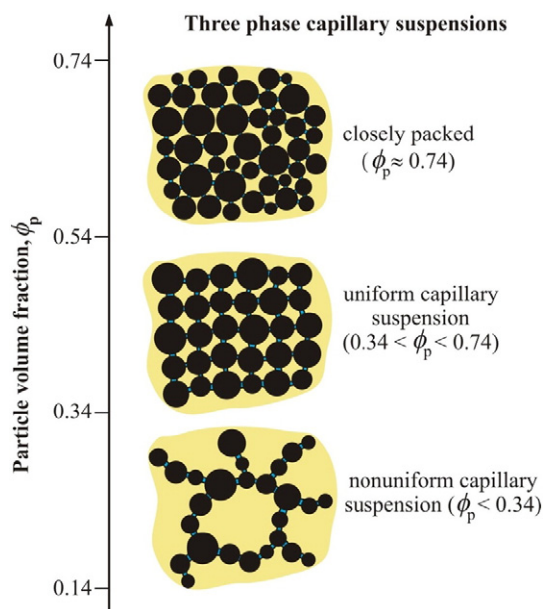


Fig. 1. Classification of the three-phase suspensions (particles/water/oil) with respect to the volume fraction of particles,  $\phi_p$  (pendular state).

An important parameter characterizing the capillary suspensions is the volume fraction of the preferentially wetting (inner) liquid relative to the total volume of the liquid phases (degree of saturation with the inner liquid) [13]:

$$S_i = \frac{\phi_i}{\phi_w + \phi_{oil}}, \quad i = w, oil \quad (1)$$

Here,  $\phi_w$  and  $\phi_{oil}$  are, respectively, the volume fractions of water and oil in the dispersion ( $\phi_w + \phi_{oil} + \phi_p = 1$ ). The preferentially wetting liquid could be either water or oil depending on whether the particles are hydrophilic or hydrophobic.

In the case of nonuniform suspensions,  $\phi_p < 34\%$ , different structures can be observed (Fig. 2) depending on the value of  $S_i$ . At the lowest  $S_i$  values, the particles in the network are connected by capillary bridges, i.e. the dispersion is in the *pendular state* (Fig. 2) [6]. At greater  $S_i$  values, the network splits to separate *spherical agglomerates*, where the particles are bound together by capillary forces [6,30]. At  $S_i$  close to 0.5, the particles can stabilize a bicontinuous structure, termed *bijel*, which has been a subject of increasing interest [31–34]. If  $S_i$  is further increased, particle stabilized *Pickering emulsions* could be formed [35–37]. Finally, at  $S_i$  approaching 1, the space could be spanned again by a network, but this time in the *capillary state*. The branches of this network could be considered as channels of the non-preferentially wetting liquid, which are wrapped by adsorbed particles. Hardening of the dispersion (network gelation), can be observed in both the pendular and capillary state [1,6].

The subject of our article is the rheological behavior of three-phase dispersions particles/oil/water in the vast and weakly explored concentration domain of uniform capillary suspensions,  $34\% < \phi_p < 74\%$ ; see Fig. 1. Our study is focused on the *pendular state*, which possesses the remarkable property that the addition of a minimal amount of the inner liquid phase leads to strong solidification of the dispersion owing to the particle interconnection with capillary bridges. When such dispersion is subjected to deformation, three types of rheological response are observed: (i) quasielastic; (ii) transitional, characterized by the yield stress, and (iii) viscoelastic. Our study is focused on the experimental study of the *yield stress* and its interpretation on the basis of the computed capillary-bridge force. The greater the yield stress, the stronger the solidified dispersion.

### Nonuniform capillary suspensions

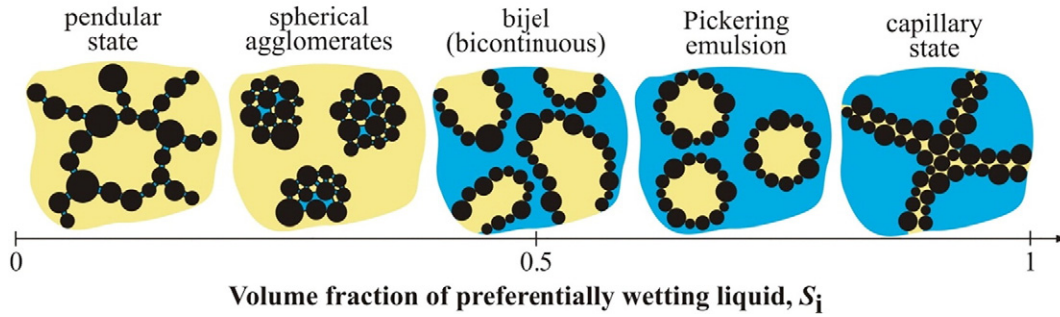


Fig. 2. Changes in the morphology of the nonuniform three-phase suspensions (particles/water/oil) with respect to the volume fraction of the preferentially wetting liquid,  $S_i$ ; after Koos [6].

#### 1.3. Number of capillary bridges per particle

As already mentioned, in the pendular state the capillary bridges are formed around the zones of contact of neighboring particles. If the particles are uniformly distributed in space, the number of nearest neighbors (the coordination number),  $n$ , depends on the particle volume fraction,  $\phi_p$ .

To illustrate that, let us consider regular lattices from monodisperse spherical particles (Fig. 3a). The lowest number of nearest neighbors in a spatial lattice is  $n = 4$  for the lattice of diamond (or water ice  $I_c$ ). If we assume that the “particles” depicted in Fig. 3a represent the particle centers, but the actual neighboring particles touch each other, then the particle volume fraction will be  $\phi_p \approx 0.340$  for diamond packing. Likewise, we have  $n = 6$  and  $\phi_p \approx 0.524$  for simple cubic lattice;  $n = 8$  and  $\phi_p \approx 0.680$  for body-centered cubic lattice, and  $n = 12$  and  $\phi_p \approx 0.740$  for face-centered cubic (and hexagonal close packed) lattice [38]; see Fig. 3a.

In Fig. 3b, the symbols represent the plot of  $\phi_p$  versus  $n$  for the regular spatial lattices shown in Fig. 3a. One sees that for  $n \leq 8$  ( $\phi_p \leq 0.68$ ), the points in Fig. 3b comply with a straight line of equation  $\phi_p = 0.0857n$ . Hence, we have:

$$n = \frac{\phi_p}{0.0857} \approx 11.67 \phi_p \text{ for } \phi_p < 0.68 \quad (2)$$

In the case of capillary suspensions, we may continuously increase the particle volume fraction,  $\phi_p$ . Then, using Eq. (2) we can estimate the average number of capillary bridges per particle,  $n$ , for a capillary suspension in the pendular state.

## 2. Capillary bridges

### 2.1. Brief overview of preceding studies

Long ago, it was established that the adhesion of spherical particles to a flat plate in a humid atmosphere is due to the condensation of small aqueous capillary bridges (pendular rings) around the zones of particle/plate contacts [12,39,40]. The formation of capillary bridges is important for many experimental and practical systems and processes, such as water saturation in soils and adhesive forces in any moist unconsolidated porous media [41–44]; dispersion of pigments, wetting of powders and flocculation of particles in three-phase slurries [10,11,45,46]; densification during sintering of fine particles [47,48]; obtaining of films from latex particles [49–51]; capillary evaporation and condensation in porous media [52–54]. The action of capillary-bridge force is often detected in experiments with atomic force microscopy [55–58].

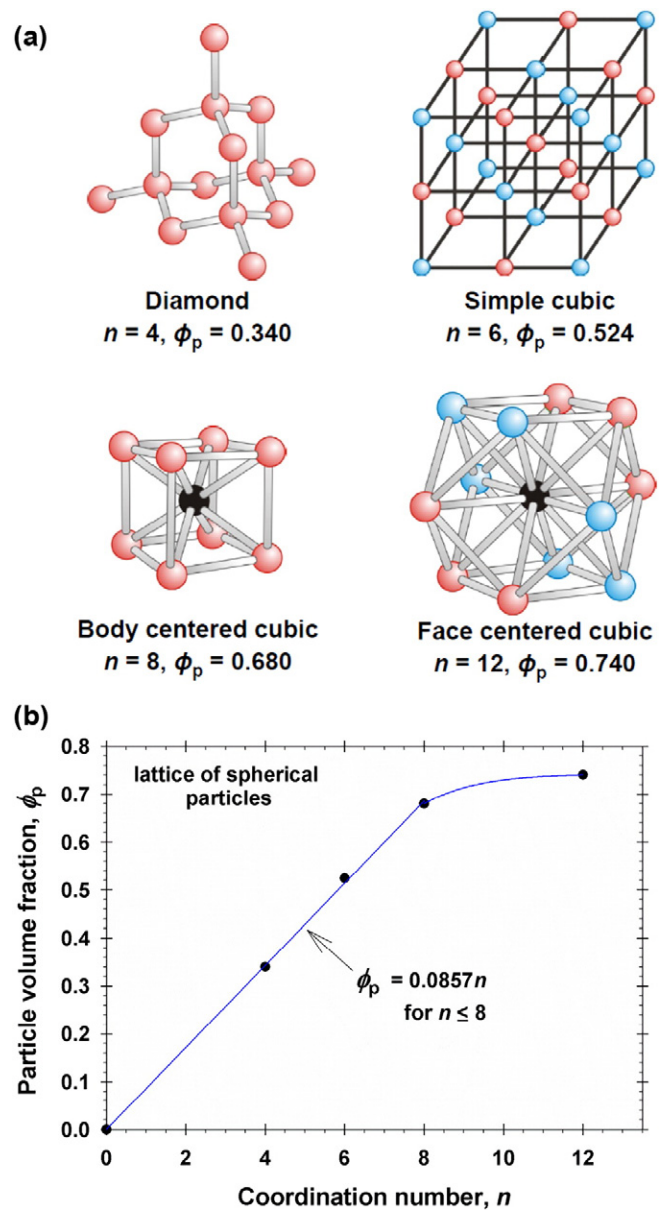


Fig. 3. (a) Regular crystal lattices with different number of closest neighbors (coordination number),  $n$ . In the case of capillary suspension, the “particles” in the figure show only the positions of the centers of the real colloidal particles;  $\phi_p$  is the volume fraction of particles supposedly their surfaces touch each other. (b) Plot of  $\phi_p$  vs.  $n$ .

The pioneering studies in this field are due to Delaunay [59], who mathematically described and classified the shapes of capillary bridges (surfaces with constant mean curvature) and to Plateau [60], who supported the theory with experimental observations and investigated the bridge stability. The instability of cylindrical capillary bridges was studied by Rayleigh [61]. The shapes of capillary bridges between two plane-parallel plates; between solid spheres and between sphere and plate were experimentally investigated in a number of works [62–65]. Exact and approximate theoretical expressions for the profile of capillary bridges and for the capillary-bridge force have been obtained in the studies of numerous authors [12,64–69]. Review articles on the stability of capillary bridges were published by Michael [70]; Myshkis et al. [71], and Lowry and Steen [72]; various specific geometries have been investigated [73–78].

In Sections 2.2 and 2.3, we overview the basic equations used in the present study to calculate the shape of capillary bridges and the interaction force between two bodies connected by capillary bridge in relation to the theoretical description of yield stress in capillary suspensions.

## 2.2. Meniscus profile and capillary bridge force

The capillary bridge between two spherical particles is axisymmetric. Its profile can be described by using cylindrical coordinates,  $z = z(r)$ ; see Fig. 4 for the notations. The meniscus profile obeys the Laplace equation of capillarity, which can be presented in the form [67,68]:

$$\frac{\sigma}{r} \frac{d}{dr} (r \sin \theta) = P_1 - P_2 \quad (3)$$

Here,  $r$  is the radial coordinate;  $\theta$  is the running slope angle;  $\sigma$  is the interfacial tension of the capillary meniscus;  $P_1$  and  $P_2$  are, respectively, the pressures inside and outside the bridge. Because the bridges in capillary suspensions are microscopic, we will neglect the effect of gravity on pressure and will consider  $P_1$  and  $P_2$  as constant quantities. Integrating Eq. (3), we obtain:

$$\sin \theta = p \frac{r}{r_0} + (1-p) \frac{r_0}{r} \quad (4)$$

where the boundary condition  $\sin \theta = 1$  at  $r = r_0$  has been used (Fig. 4);  $p$  is the dimensionless capillary pressure:

$$p = \frac{P_1 - P_2}{2\sigma} r_0 \quad (5)$$

Next, using Eq. (4) and the identities  $dz/dr = \tan \theta = \pm \sin \theta / (1 - \sin^2 \theta)^{1/2}$  we obtain:

$$\frac{dz}{dr} = \frac{pr^2 + (1-p)r_0^2}{\pm p[(r^2 - r_0^2)(r_1^2 - r^2)]^{1/2}}, \quad r_1 = \left| \frac{1-p}{p} \right| r_0 \quad (6)$$

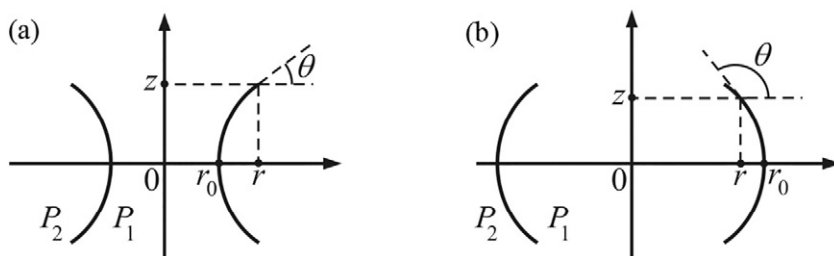


Fig. 4. Sketch of the profile of an axisymmetric capillary bridge;  $r$  is the radial coordinate; the  $z$ -axis is the axis of revolution; the midplane corresponds to  $z = 0$ , where  $r = r_0$ ;  $\theta$  is the running slope angle;  $P_1$  and  $P_2$  are the inner and outer pressures. (a) Concave capillary bridge,  $p < 0.5$  and  $r > r_0$ ; (b) Convex capillary bridge,  $p > 0.5$  and  $r < r_0$ ;  $p$  is the dimensionless capillary pressure – see Eq. (5).

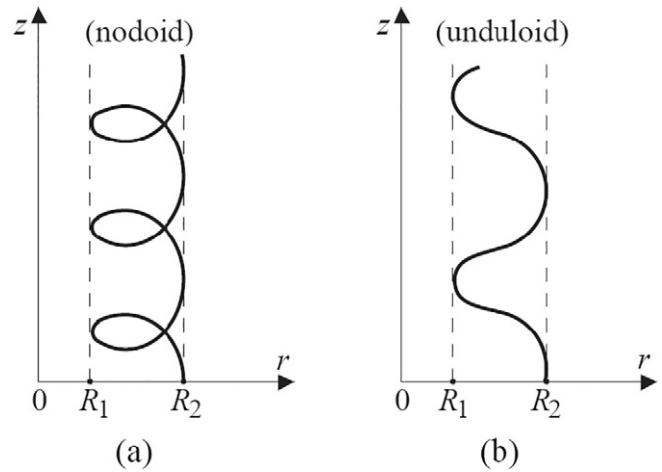


Fig. 5. The generatrix of the capillary bridge can be a part of (a) nodoid at  $p < 0$  and  $p > 1$  or (b) unduloid at  $0 < p < 1$ . These curves are confined between two vertical lines at  $r = R_1$  and  $r = R_2$ .

From the above definition of  $r_1$ , for  $p < 0.5$  we obtain  $r_1 > r_0$  and the capillary bridge is concave (with a neck). More generally, in view of Eq. (6) and Fig. 4, there are two cases:

$$\begin{aligned} -\infty < p < 0.5, \quad r_0 < r < r_1 & \text{(concave capillary bridge)} \\ 0.5 < p < +\infty, \quad r_1 < r < r_0 & \text{(convex capillary bridge)} \end{aligned} \quad (7)$$

In the special case  $p = 0.5$ , we have  $r_1 = r_0$ , and then the capillary bridge has the form of cylinder.

The denominator in Eq. (6) indicates that the meniscus profile has two vertical asymptotes (with  $dz/dr = \pm \infty$ ), at  $r = r_0$  and  $r = r_1$ . In 1841, Delaunay has shown that for  $0 < p < 1$  the meniscus profile described by Eq. (6) is a part of an “undulated” curve with inflection points, called *unduloid*, whereas for  $p < 0$  and  $p > 1$  the profile is described by a self-intersecting curve without inflection points, called *nodoid*; see Fig. 5. In this figure,  $R_1 = r_0$  and  $R_2 = r_1$  for concave bridge, whereas  $R_1 = r_1$  and  $R_2 = r_0$  for convex bridge.

The limiting case  $p = 1$  corresponds to *sphere* with two equal principal curvatures ( $c_1 = c_2$ ), whereas the limiting case  $p = 0$  (zero capillary pressure) corresponds to *catenoid* (pseudosphere), for which the two principal curvatures have equal magnitudes but opposite signs ( $c_1 = -c_2$ ). In the general case, the solution of Eq. (6) can be expressed in terms of elliptic integrals; for details, see e.g. Ref. [67,68].

Trying different methods to compute the meniscus profile, we found that the most convenient way is to integrate Eq. (6) numerically. For this goal, to remove the singularity at  $r = r_0$ , we introduced a new variable,  $x$ , as follows:

$$\begin{aligned} r &= r_0(1 + x^2) \text{ for concave capillary bridge} \\ r &= r_0(1 - x^2) \text{ for convex capillary bridge} \end{aligned} \quad (8)$$

In the case of *concave* capillary bridge ( $p < 0.5$ ), substituting  $r_1$  from its definition and  $r$  from Eq. (8), and integrating Eq. (6) we obtain:

$$z(x) = 2r_0 \int_0^x \frac{1 + p\xi^2(2 + \xi^2)}{[(2 + \xi^2)(1 - 2p - 2p^2\xi^2 - p^2\xi^4)]^{1/2}} d\xi \quad (9)$$

where  $\xi$  is an integration variable. Likewise, for *convex* capillary bridge ( $p > 0.5$ ), the integration of Eq. (6) yields:

$$z(x) = 2r_0 \int_0^x \frac{1 - p\xi^2(2 - \xi^2)}{[(2 - \xi^2)(2p - 1 - 2p^2\xi^2 + p^2\xi^4)]^{1/2}} d\xi \quad (10)$$

The numerical integration in Eqs. (9) and (10) was carried out by using the Simpson method. These two equations describe the upper part of the bridge (for  $z \geq 0$ ; see Fig. 4); the lower part can be obtained by reflection because of the symmetry with respect to the midplane,  $z = 0$ .

The meniscus profile should satisfy a certain boundary condition,  $z = z_c$  and  $\theta = \theta_c$  for  $r = r_c$ , where  $(r_c, z_c)$  determines the position of the three-phase contact line on the solid surface;  $\theta_c$  is the meniscus slope angle at the contact line. In our computational procedure, described in Appendix A,  $r_0$  is varied until the boundary condition is satisfied. At that,  $p$  is calculated from Eq. (4) with  $r = r_c$  and  $\theta = \theta_c$ :

$$p = \frac{r_0^2 - r_0 r_c \sin \theta_c}{r_0^2 - r_c^2} \quad (11)$$

The meniscus volume and surface area can be also calculated using Eqs. (A.10) and (A.11) in Appendix A.

Having determined  $p$ , we can calculate the *capillary-bridge force*,  $F_{\text{cap}}$ , using the expression:

$$F_{\text{cap}} = 2\pi r_0 \sigma - (P_1 - P_2) \pi r_0^2 = 2\pi r_0 \sigma (1 - p) \quad (12)$$

Eq. (12) can be derived by force-balance considerations; see e.g. Ref. [68]. The term  $2\pi r_0 \sigma$  represents the contribution of the meniscus interfacial tension, whereas the term  $(P_1 - P_2) \pi r_0^2$  is the contribution of the capillary pressure.

### 2.3. The sequence of capillary bridges

With the increase of the dimensionless capillary pressure,  $p$ , one observes a sequence of capillary-bridge shapes [68], called also Delaunay profiles [59,76], which are illustrated in Fig. 6. For  $-\infty < p < 0$ , the generatrix of the meniscus profile is a *concave nodoid*. In this case, the contributions of interfacial tension and capillary pressure to  $F_{\text{cap}}$  have the same sign, and the capillary-bridge force is the maximal; see Eq. (12). These are the only bridges, in which the inner pressure  $P_1$  is lower than the outer pressure  $P_2$ .

For  $p = 0$ , the meniscus shape is a *pseudosphere* (*catenoid*), which can be expressed in terms of elementary functions:

$$z(r) = \pm r_0 \ln \left[ r/r_0 + \sqrt{(r/r_0)^2 - 1} \right] \quad (13)$$

The pressures inside and outside the bridge are equal ( $P_1 = P_2$ ), so that  $F_{\text{cap}}$  is determined solely by the interfacial-tension term; see Eq. (12).

For  $0 < p < 0.5$ , the meniscus shape is a *concave unduloid*; for  $p = 0.5$  – *cylinder*, and for  $0.5 < p < 1$  – *convex unduloid*. For all these profiles, the capillary-pressure contribution to  $F_{\text{cap}}$  corresponds to repulsion (the inner pressure  $P_1$  is higher than the outer pressure  $P_2$ ). However, the interfacial tension term in Eq. (12) still prevails so that the net capillary-bridge force is attractive.

For  $p = 1$ , the meniscus profile is a *sphere* (the generatrix is circular arc); the interfacial-tension and capillary-pressure terms in Eq. (12) exactly counterbalance each other, so that the net capillary-bridge force is zero,  $F_{\text{cap}} = 0$ .

For  $p > 1$ , the meniscus profile is described by a *convex nodoid*; the inner pressure  $P_1$  is higher than the outer pressure  $P_2$ , and the capillary-pressure term in Eq. (12) prevails over the interfacial-tension term, so that the net capillary-bridge force corresponds to *repulsion*.

The profile of the capillary bridge may have an inflection point, which is related to its stability. At the inflection point,  $r = r_i$ , the derivative of the running slope angle with respect to distance should be zero. Taking the derivative of Eq. (4), we obtain  $0 = p/r_0 - (1 - p)r_0 / r_i^2$ , that is:

$$r_i^2 = \frac{1 - p}{p} r_0^2 = r_0 r_1 \quad (14)$$

The above equation is satisfied only for  $0 < p < 1$ , i.e. only *unduloidal* profiles may have inflection points (see Figs. 5 and 6). Because the real meniscus profile is only a *part* of unduloid, not every unduloidal bridge will have inflection points. For symmetric capillary bridges between *parallel planes* it has been shown that no such bridge can have an inflection point in its profile and be stable [73,74]. Then, stable (without inflection points) are the bridges, for which

$$\begin{aligned} r_i > r_c & \text{ for } 0 < p < 0.5 \text{ (concave unduloids)} \\ r_i < r_c & \text{ for } 0.5 < p < 1 \text{ (convex unduloids)} \end{aligned} \quad (15)$$

For symmetric capillary bridges between two parallel planes it was established [65] that the dependence of the equilibrium length  $h$  of the capillary bridge as a function of the contact line radius,  $r_c$ , has a maximum,  $h_{\text{max}}$ , at fixed bridge volume and contact angle,  $\theta_c$ . Upon extension of the bridge, for  $h > h_{\text{max}}$  the bridge becomes unstable, evolves in dynamic regime and eventually breaks [65,78].

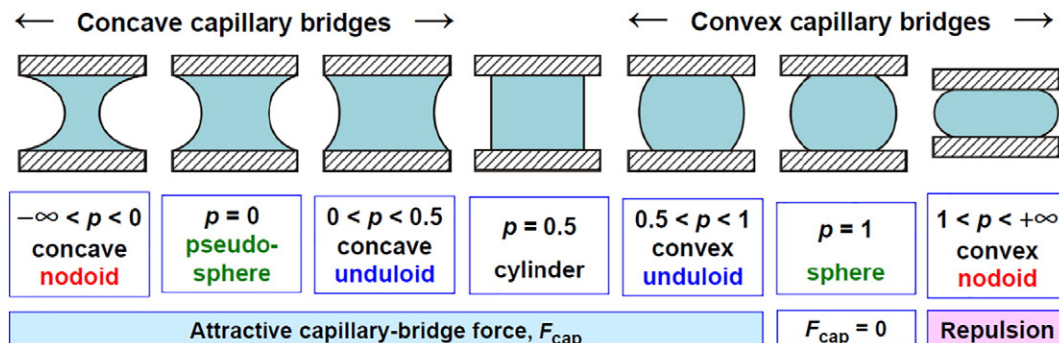


Fig. 6. Sequence of capillary bridge profiles for increasing dimensionless capillary pressure,  $p$ ; after Ref. [68].

In the case of symmetric capillary bridges between two identical spherical particles, which are not in contact, Vogel [75,76] proved that the convex bridges are *unstable* for  $1 < p < +\infty$  (convex nodoids), and *stable* for  $0.5 < p \leq 1$  (convex unduloid or sphere). It was proven that if the cylindrical bridge between *spherical particles* is stable, then the unduloidal bridges near cylinder are also stable, even if they have inflection points [73]. In other words, the conditions for stability of bridges between two parallel planes and between two spherical particles can be different.

For symmetrical capillary bridges between two identical spherical beads *in contact*, it was established that *no* stable bridges exist if the contact angle is  $\theta_c \geq \pi/2$  [77]. This theorem implies that in the capillary suspensions, the formation of pendular rings is expected only from the preferentially wetting liquid, for which  $\theta_c < \pi/2$ .

### 3. Experiments with particle/oil/water suspensions

#### 3.1. Experimental materials and procedures

In our experiments, we used hydrophilic silica particles Excelca UF320 produced by Tokuyama Corp., Japan, by melting of synthetic  $\text{SiO}_2$  (density 2.2 g/cm<sup>3</sup>). The particles were spherical, polydisperse, with low surface roughness and average particle diameter 3.8  $\mu\text{m}$ ; see Fig. S1 in Appendix B and Ref. [79]. The particles were hydrophobized with hexamethyldisilazane (HMDS, 99%, Sigma Aldrich). The silica particles were heated to 800 °C for 30 min. After annealing in a desiccator with reduced humidity, the particles were brought into contact with vapor of HMDS under permanent stirring for 16 h.

As oily phases, hexadecane (C16) and soybean oil (SBO) were used. Hexadecane (Merck – 8.20633) has a density of 773 g/L and viscosity 3.0 mPa·s. Before the experiments, the oil was purified by passing it three times through a glass column filled with Silica gel (Fluka – C989Q77) and Florisil adsorbent (activated magnesium silicate, Sigma-Aldrich). To check the degree of hexadecane purification, we measured its interfacial tension,  $\sigma$ , against pure water using a pendant drop tensiometer (instrument DSA30, Krüss GmbH, Germany). The measured value of  $\sigma$  was 52 mN/m (the literature value for hexadecane at room temperature). The soybean oil (SBO) from a local producer was purified by passing through a column filled with Silica gel and Florisil adsorbent. The measured value of  $\sigma$  was 30 mN/m (typical value for pure SBO) and it did not decrease by >0.2 mN/m within 60 min. The measured viscosity of purified SBO at room temperature was 50 mPa·s.

For preparation of all suspensions we used deionized water (Elix purification system, Millipore). No surfactants have been used. The aqueous phase contained dissolved 0.5 M NaCl (Merck) added to suppress the electrostatic repulsion between the solid particles and oil drops across the water phase. All experiments have been carried out at a room temperature of  $25 \pm 1$  °C.

The three-phase contact angle was measured with bigger particles (of radius 200–300  $\mu\text{m}$ ), hydrophobized in the same manner. The particles were floating on the oil/water interface and the contact angle was determined goniometrically, by side-view observations [80,81]. In the case of SBO, the measured contact angle was  $\alpha = 12^\circ$  across the SBO ( $168^\circ$  across the water). In the case of C16, the measured contact angle was  $\alpha = 70^\circ$  across the hexadecane ( $110^\circ$  across the water). In the case of capillary bridges, it is convenient to use the contact angle  $\alpha$  measured across the bridge phase (in our case, across the oil phase).

The HMDS-treated silica particles were so hydrophobic that they did not enter the aqueous phase when placed on the air/water interface and subjected to agitation. (For this reason, we have no data for the rheology of suspension of hydrophobic particles in water without oil.) If the particles and oil were simultaneously placed on the air/water interface, then it was possible to bring them into the aqueous phase by agitation with a propeller stirrer (Proxxon FBS 12/EF) with blending element

from frappé mixer. The homogenization was performed at a rotation speed of 5000 rpm for 5 min.

#### 3.2. Experimental method

The rheological measurements were carried out using a rotational rheometer Bohlin Gemini, Malvern, UK, with geometry of two parallel disks (Fig. 7a). The upper disk is rotating, whereas the lower disk is immobile. Sheets of hydrophilic sandpaper of average particle diameter  $\approx 12.6$   $\mu\text{m}$  were glued to both disks to prevent the appearance of wall slip. The disk radius was  $R = 20$  mm. The investigated suspension was sandwiched between the two disks at a gap distance of 2 mm. To prevent evaporation of water from the suspensions, on top of the upper plate a ring-shaped vessel filled with water was placed and the portion of the setup with the two disks was closed under a cover.

To characterize the hardness of dispersions, we used the *stress-control regime* of the rheometer. At each fixed value of the applied shear stress,  $\tau$ , the strain, characterized by the rotation angle  $\psi$ , was measured; see Fig. 7b. By definition,  $\tau = 3M/(2\pi R^3)$  is an average value of the mechanical stress  $\tau_{z\varphi}$  acting on the rotating disk;  $M$  is the applied force moment (torque); see Section 5.1 for more details.

#### 3.3. Experimental results

As seen in Fig. 7b, at the lower  $\tau$  values the rotation angle  $\psi$  slowly increases. This is a *quasi-elastic regime* of deformation. The values of  $\psi$  in this regime, up to 0.1 rad ( $5.7^\circ$ ) are too large to be

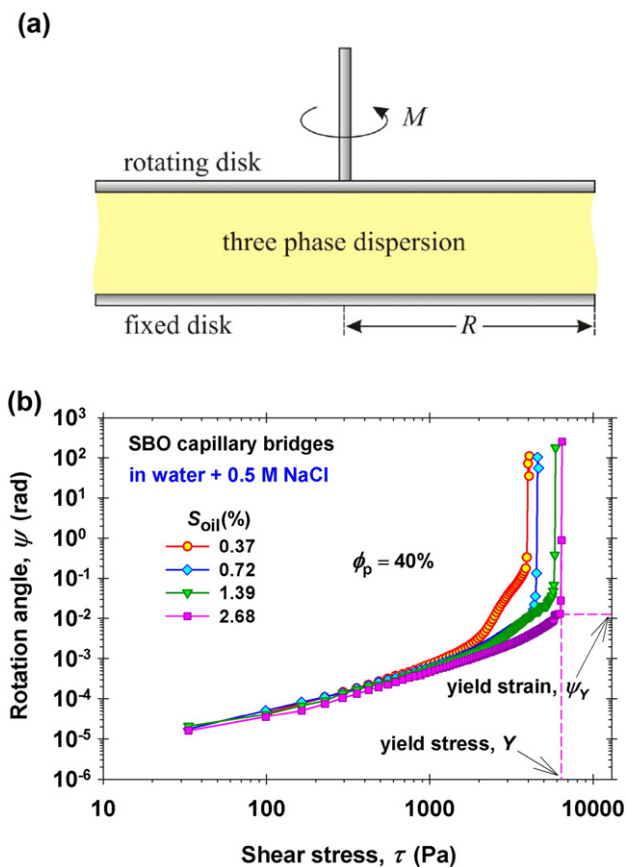


Fig. 7. (a) Sketch of the used rotational rheometer with two parallel disks;  $R$  is the disk radius and  $M$  is the applied force moment (torque). (b) Experimental data for the displacement angle,  $\psi$ , vs. the applied stress,  $\tau = 3M/(2\pi R^3)$ , for four different values of  $S_{\text{oil}}$ . The yield stress,  $Y$ , is determined from the vertical portion of the experimental curve.

explained in terms of elastic deformation of the solid (in our case  $\text{SiO}_2$ ) particles, as proposed by Rumpf and Schubert [4]. This quasi-elastic deformation can be explained by extension of the capillary bridges upon shearing; see Section 4.1. At a certain value,  $\tau = Y$ , the angle  $\psi$  abruptly increases because the elastic limit has been reached. This value is identified with the *yield stress*,  $Y$ . The respective

value of the rotation angle,  $\psi_Y$ , will be termed *yield strain*. In our experiments,  $Y$  was measured as a function of the relative volume fraction of the inner liquid (in our case – oil),  $S_{\text{oil}}$ , at different particle volume fractions,  $\phi_p$ .

Fig. 8 shows our data for  $Y$  vs.  $S_{\text{oil}}$  for soybean oil (SBO) as inner phase at  $\phi_p = 30\%$ ,  $40\%$  and  $45\%$ . (At  $\phi_p = 50\%$ , the dispersion was too hard and inappropriate for investigation with the used rheometer.) Each point is average from at least three measurements, which have been carried out with separately prepared suspension samples of the same  $S_{\text{oil}}$  and  $\phi_p$ . The data indicate that the yield stress,  $Y$ , increases with the rise of both  $S_{\text{oil}}$  and  $\phi_p$ . For example, at  $S_{\text{oil}} = 5\%$  we have  $Y = 3955$ ,  $5644$  and  $6506$  Pa for  $\phi_p = 30\%$ ,  $40\%$  and  $45\%$ , respectively (the values are taken from the data fit). Such increase of  $Y$  with the rise of  $\phi_p$  has been observed also for other jammed suspensions [82]. The error bars in Fig. 8 illustrate the reproducibility of these experiments, which is the range from 5% to 10%. At  $S_{\text{oil}} \geq 8\text{--}10\%$ , the dependence of  $Y$  on  $S_{\text{oil}}$  becomes irregular, which can be interpreted as a transition from the pendular to the funicular state due to overlap of neighboring capillary bridges (Fig. 1). At  $S_{\text{oil}} \geq 15\text{--}17\%$ , phase separation is observed: the dispersion is decomposed to aqueous and oil phases; the hydrophobic particles are located in the oily phase. At that, the system becomes fluid and  $Y = 0$ .

Fig. 9 shows analogous data, but for capillary bridges from hexadecane (C16), instead of SBO. Because these experiments are much time and labor consuming, in this case we carried out only one experiment for each  $S_{\text{oil}}$  and  $\phi_p$ . (The reproducibility of this type of experiments has been already estimated in Fig. 8.) Insofar as the oil/water interfacial tension for C16 is higher than that for SBO (52 vs. 30 mN/m), one could expect greater capillary-bridge force and greater yields stress,  $Y$ , for C16. In contrast with this expectation, the experiment gives lower  $Y$  for C16. For example, from Figs. 8c and 9b we find that at  $S_{\text{oil}} = 5\%$  and  $\phi_p = 45\%$ , we have  $Y = 6506$  Pa for SBO bridges vs.  $Y = 2162$  Pa for C16 bridges.

In other words, the suspensions with inner phase of C16 are considerably softer than those with SBO. As discussed below, the main reason for this difference is the greater contact angle  $\alpha = 70^\circ$  for C16 (vs.  $\alpha = 12^\circ$  for SBO). The fact that the dispersions with C16 are softer allowed us to carry out experiments at higher particle volume fractions, up to  $\phi_p = 55\%$  (Fig. 9d). Again, some scattering of the data points at the higher  $S_{\text{oil}}$  values can be explained with a transition from pendular to funicular state. Upon a further increase of  $S_{\text{oil}}$ , phase separation is observed, as in the case with SBO (see above).

#### 4. Theoretical description of the yield stress

From a physical viewpoint, at a given temperature the yield stress  $Y$  of a capillary suspension is expected to depend on five parameters:

$$Y = Y(S_i, \phi_p, \sigma, a, \alpha) \quad (16)$$

where as usual,  $S_i$ , is the relative volume fraction of the inner liquid (bridge) phase;  $\phi_p$  is the particle volume fraction;  $\sigma$  is the interfacial tension;  $a$  is the particle radius and  $\alpha$  is the three-phase contact angle measured across the bridge phase. Until now, the explicit form of the above dependence has not been found; see e.g. Ref. [3]. Our goal in the present section is to obtain the dependence in Eq. (16) in explicit form. For this goal, let us first consider the physical origin of the yield stress.

##### 4.1. The elastic limit upon shear deformation – general approach

Here, we will follow an approach similar to that applied to a jammed particle monolayer at a liquid interface [83]. Let us consider two neighboring particles, A and B, in a suspension that interact via central force,  $F$ , which could be, for example, of van-der-Waals, electrostatic,

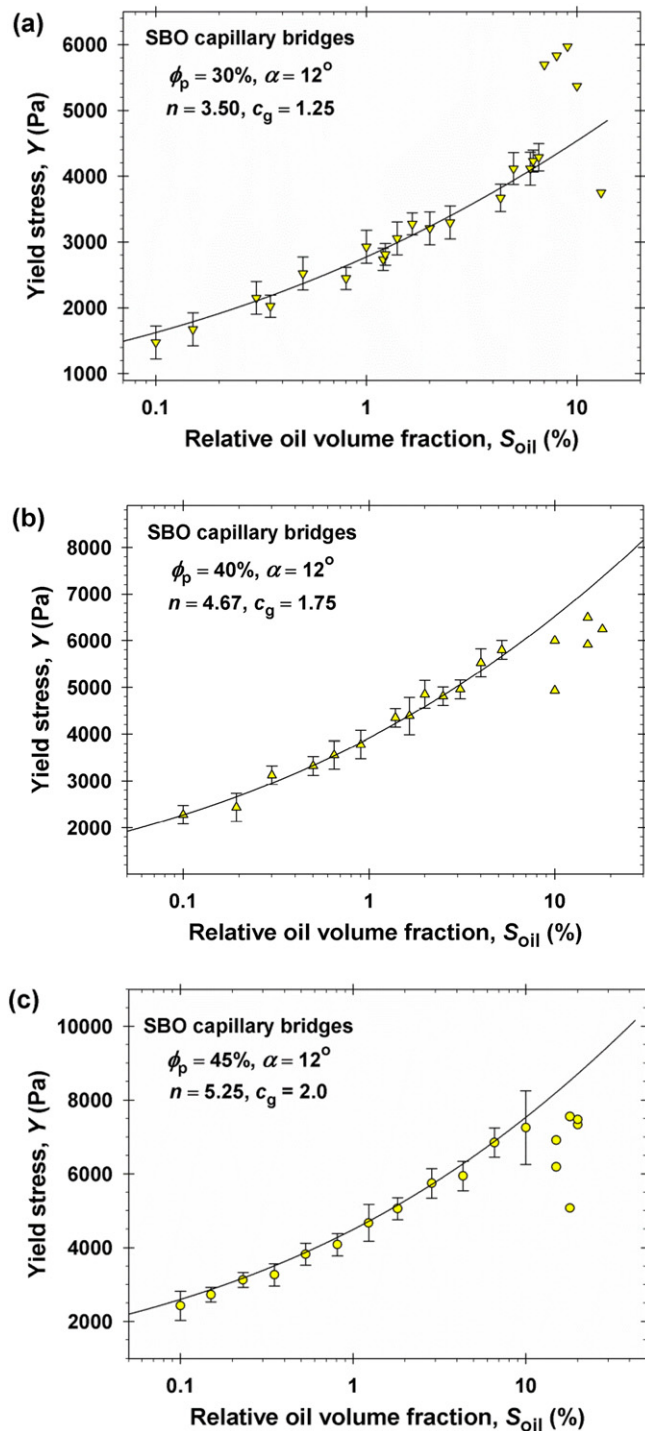
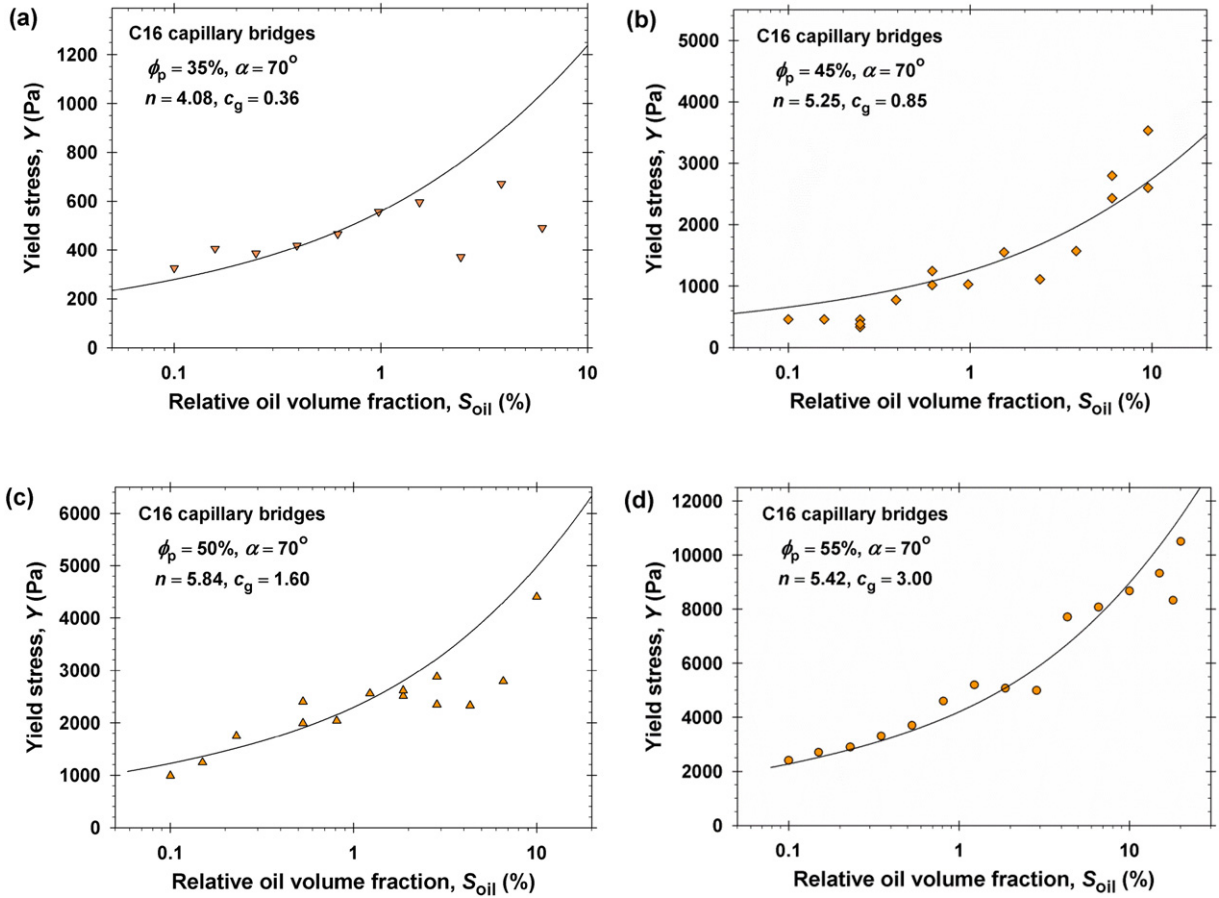


Fig. 8. Suspension with capillary bridges from soybean oil (SBO) in water: Plot of the measured yield stress,  $Y$ , vs. the relative oil volume fraction,  $S_{\text{oil}}$ , for hydrophobized silica particles of contact angle  $\alpha = 12^\circ$  across the SBO at particle volume fractions (a)  $\phi_p = 30\%$ ; (b)  $\phi_p = 40\%$ , and (c)  $\phi_p = 45\%$ . The average number of capillary bridges per particle,  $n$ , is estimated from Eq. (2). The solid lines are fits by means of the theoretical model. The geometrical coefficient,  $c_g$ , is determined from the fit (details in the text).





**Fig. 9.** Suspension with capillary bridges from n-hexadecane (C16) in water: Plot of the measured yield stress,  $Y$ , vs. the relative oil volume fraction,  $S_{oil}$ , for hydrophobized silica particles of contact angle  $\alpha = 70^\circ$  across the C16 at particle volume fractions (a)  $\phi_p = 35\%$ ; (b)  $\phi_p = 45\%$ ; (c)  $\phi_p = 50\%$ , and (d)  $\phi_p = 55\%$ . The average number of capillary bridges per particle,  $n$ , is estimated from Eq. (2). The solid lines are fits by means of the theoretical model. The geometrical coefficient,  $c_g$ , is determined from the fit (details in the text).

and/or capillary-bridge (Fig. 10a) origin. A small shear deformation in the suspension along the  $y$ -axis leads to a small displacement  $\Delta y$  of the particle B (Fig. 10b). This displacement gives rise to an increase of

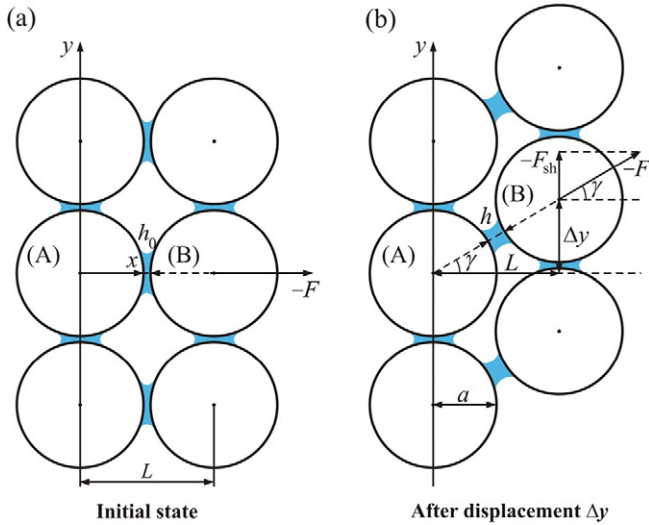


**Fig. 10.** Sketch of suspension from spherical particles of radius  $a$  connected by capillary bridges; (a) the initial state; (b) after a shear deformation at displacement  $\Delta y$  along the  $y$ -axis;  $L$  is the distance between two layers of particles;  $\gamma$  is the shearing angle;  $h_0$  and  $h$  are the lengths of the capillary bridge before and after the shearing;  $F$  is the force of interaction between the particles A and B;  $F_{sh} = F \sin \gamma$  is the projection of  $F$  on the shear plane.

the surface-to-surface distance between the particles A and B from  $h_0$  to  $h$ . After the displacement, the central force  $F$  has non-zero projection on the shear plane:

$$F_{sh} \equiv F(h) \sin \gamma = F(h) \frac{\varepsilon}{(1 + \varepsilon^2)^{1/2}} \quad (17)$$

where  $\varepsilon = \Delta y/L = \tan \gamma$  (Fig. 10b). Using series expansions for small  $\varepsilon$ , we obtain:

$$\frac{\varepsilon}{(1 + \varepsilon^2)^{1/2}} = \varepsilon - \frac{1}{2} \varepsilon^3 + O(\varepsilon^5) \quad (18)$$

$$h = [L^2 + (\Delta y)^2]^{1/2} - 2a = L(1 + \varepsilon^2)^{1/2} - 2a = h_0 + \frac{1}{2} L \varepsilon^2 + O(\varepsilon^4) \quad (19)$$

$$F(h) = F(h_0) - \frac{1}{2} |F'_h| L \varepsilon^2 + O(\varepsilon^4), \quad F'_h = \left. \frac{dF}{dh} \right|_{h=h_0} \quad (20)$$

where we have assumed that the derivative  $F'_h$  is negative, i.e. that the magnitude of the net attractive force decreases with the distance  $h$ . Substituting Eqs. (18) and (20) into Eq. (17), we derive:

$$F_{sh}(\varepsilon) \approx F(h_0) \varepsilon - \frac{1}{2} [F(h_0) + |F'_h| L] \varepsilon^3 \quad (21)$$

where higher-order terms with respect to  $\varepsilon$  have been neglected. The function  $F_{sh}(\varepsilon)$  has a maximum at  $\varepsilon = \varepsilon_m$ , which is determined from the relation:

$$\varepsilon_m = \frac{(2/3)^{1/2}}{[1 + |F'_h|L/F(h_0)]^{1/2}} \quad (22)$$

$$F_{sh, \max} \approx \frac{2}{3} F(h_0) \varepsilon_m \quad (23)$$

For  $F_{sh} < F_{sh, \max}$ , the system can counterbalance the applied external shear stress, i.e. we are dealing with quasi-elastic regime; see Figs. 7b. The maximal value  $F_{sh, \max}$  corresponds to the *elastic limit* and is related to the *yield stress*. Note that in the stress-control regime (used in our experiments) the yield stress is related to the maximum of  $F_{sh}(\varepsilon)$ , rather than to the end-of-equilibrium point of an extended capillary bridge (Fig. 11b).

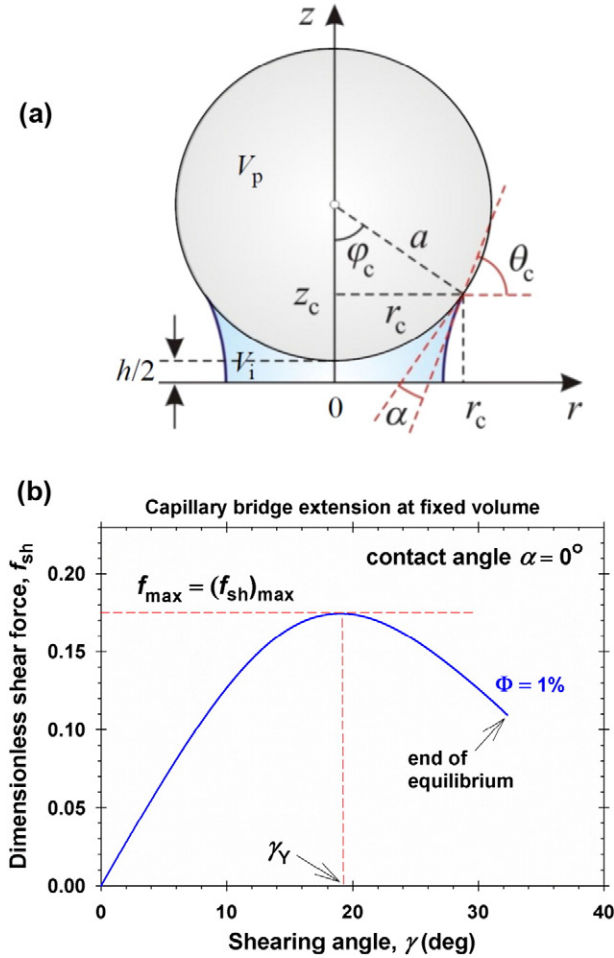


**Fig. 11.** (a) Capillary bridge between two particles of equal size, like those in Fig. 10; half of the bridge is shown;  $h$  is the closest particle surface-to-surface distance;  $\alpha$  is the three-phase contact angle measured across the bridge phase;  $r_c$  and  $z_c$  are the coordinates of the three-phase contact line;  $\varphi_c$  is the respective central angle;  $\theta_c = \alpha + \varphi_c$  is the meniscus slope at the contact line;  $V_p$  is the particle volume;  $V_i$  is the volume of the “inner liquid” in the half-bridge;  $\Phi = V_i/V_p$  is the dimensionless bridge volume. (b) Plot of the dimensionless shear-response force,  $f_{sh}$ , vs. the shearing angle,  $\gamma$ , calculated for a capillary bridge that is subjected to extension (increase of  $h$ ) at fixed  $\Phi = 1\%$  and  $\alpha = 0$ . The bridge cannot resist external force greater than  $f_{\max}$ ;  $\gamma_Y$  is the respective threshold value of the shearing angle (yield strain).

#### 4.2. Expression for the yield stress

In view of Fig. 10b, the shear stress,  $\tau$ , that is the force per unit area of the  $yz$ -plane, can be expressed in the form:

$$\tau = c_g \frac{F_{sh}}{A_1} \quad (24)$$

$A_1$  is the area per particle in the shear plane and  $c_g$  is a geometrical coefficient, which accounts for the number of capillary bridges per particle and their orientation relative to the shear plane. For the configuration in Fig. 10 [simple cubic lattice, (100) shear plane], we have  $c_g = 1$  (the area per bridge coincides with the area per particle) and  $A_1 = 4a^2$ .

In the general case, the volume per particle in the suspension could be modelled as the volume of a polyhedron containing the particle, which could be approximated with a sphere of radius  $R_1$  that has the same volume:

$$\frac{4}{3}\pi R_1^3 = \frac{4}{3}\pi a^3 \Rightarrow R_1 = \frac{a}{\phi_p^{1/3}} \quad (25)$$

Then,  $A_1$  can be estimated as the area of the great circle of this sphere:

$$A_1 = \pi R_1^2 = \frac{\pi a^2}{\phi_p^{2/3}} \quad (26)$$

The last equation can be considered as a definition of  $A_1$ , which affects also the definition of  $c_g$ . The substitution of  $A_1$  from Eq. (26) into Eq. (24) yields:

$$\tau = c_g \phi_p^{2/3} \frac{F_{sh}}{\pi a^2} \quad (27)$$

Insofar as the yield stress  $Y$  is related to the maximal value of  $F_{sh}$  (Fig. 11b), from Eq. (27) we obtain:

$$Y = c_g \phi_p^{2/3} \frac{F_{sh, \max}}{\pi a^2} \quad (28)$$

In the special case when *only* capillary-bridge force is acting between the particles, that is  $F = F_{cap}$ , it is convenient to work in terms of the following dimensionless quantities:

$$f_{cap} = \frac{F_{cap}}{2\pi a\sigma}, \quad f_{sh} = \frac{F_{sh}}{2\pi a\sigma}, \quad f_{\max} = (f_{sh})_{\max} \quad (29)$$

where, as usual,  $\sigma$  is the interfacial tension;  $f_{cap}$  and  $f_{sh}$  are the dimensionless capillary force and its projection on the shear plane;  $f_{\max}$  is the maximal value of  $f_{sh}$ . In view of Eqs. (28) and (29), the yield stress can be presented in the form:

$$Y = \frac{2\sigma}{a} c_g \phi_p^{2/3} f_{\max}(\Phi, \alpha) \quad (30)$$

Eq. (30) shows that  $Y$  scales with the capillary pressure  $2\sigma/a$ . In other words,  $Y$  increases with the rise of the interfacial tension,  $\sigma$ , and with the decrease of the particle radius,  $a$ . The fact that  $Y \propto 1/a$  has been found experimentally [14]. The term  $c_g \phi_p^{2/3}$  is proportional to the number of bridges per unit area of the shear plane;  $c_g$  may depend not only on geometrical factors, but also on dynamic factors related to the bridge formation during the stirring/preparation of the suspension (see below). In this article,  $c_g$  is determined as an adjustable parameter from the fits of experimental data for  $Y$ .  $f_{sh, \max} \equiv f_{\max}(\Phi, \alpha)$  is a dimensionless universal function that has been computed using the exact theory of capillary bridges and tabulated; see Table C1 in

Appendix C. Using the tabulated data and four-point interpolation, one can easily compute  $f_{\max}(\Phi, \alpha)$  for every values of  $\Phi$  and  $\alpha$  (details in Appendix C). As usual,  $\alpha$  is the contact angle measured across the bridge phase; by definition, the dimensionless bridge volume is  $\Phi = V_{\text{bridge}} / (2V_p) = V_i / V_p$ , where  $V_p$  is the particle volume and  $V_i = V_{\text{bridge}} / 2$  is the volume of the “inner liquid” in the half-bridge (Fig. 11a). In other words,  $\Phi$  is the bridge volume scaled with the volume of the two adjacent particles.

To find a relation between  $\Phi$  and the experimental volume fraction,  $S_i$ , we will assume that capillary bridges are formed between each given particle and all its nearest neighbors. If  $n$  is the average number of nearest neighbors, then  $\Phi$  and  $\phi_i/\phi_p$  are related by the expression:

$$n\Phi = \frac{\phi_i}{\phi_p} \quad (i = w, \text{ oil}) \quad (31)$$

where  $\phi_i$  is the volume fraction of the inner liquid in the dispersion. In view of Eq. (1), we have:

$$S_i \equiv \frac{\phi_i}{\phi_w + \phi_{\text{oil}}} = \frac{\phi_i}{1 - \phi_p} = \frac{\phi_i/\phi_p}{1/\phi_p - 1} \quad (32)$$

Combining Eqs. (31) and (32), we obtain the following relationships:

$$S_i = \frac{n\Phi}{1/\phi_p - 1} \Leftrightarrow \Phi = \frac{1 - \phi_p}{n\phi_p} S_i \quad (i = w, \text{ oil}) \quad (33)$$

When comparing theory and experiment, Eqs. (2) and (33) are used to calculate  $n$  and  $\Phi$  from the experimental quantities  $\phi_p$  and  $S_i$ , and then the yield stress is calculated from Eq. (30).

Note that  $\tau$  and  $Y$  in Eqs. (27) and (28) represent *local* shear stresses. In contrast, the shear stress registered by the rotational rheometer is an *integral* average effect of the shear stresses acting on the whole area of the rotating disk (Fig. 7a). The relation between the theoretical and experimental yield stress is considered in Section 5.1.

In Eq. (28), the theoretical value of  $Y$  can be estimated by substituting  $f_{\max} = f_{\text{sh}, \max}$  from Eq. (23). However, the series expansions used to derive Eq. (23) have a limited validity. In Section 4.3, to ensure correct quantitative description of the yield stress in capillary suspensions,  $f_{\max}$  is calculated using the exact theory of capillary bridges.

#### 4.3. Exact numerical results

The computational procedure based on the exact theory of capillary bridges between spherical particles is described in Appendix A. It allows one to calculate the meniscus profile  $z(r)$  at given values of three parameters, which can be (i)  $r_c$ ,  $h$ , and  $\alpha$ , or (ii)  $h$ ,  $\Phi$  and  $\alpha$ . Illustrative meniscus profiles  $z(r)$  at various  $r_c$  values and fixed  $\alpha = 70^\circ$  and  $h = 0$  (pendular rings) are shown in Fig. S2 in Appendix B. In addition, meniscus profiles  $z(r)$  at various  $h$  values, fixed  $\Phi$  and two fixed contact angles,  $\alpha = 12^\circ$  and  $70^\circ$ , are shown in Fig. S3. We recall that  $\alpha = 12^\circ$  and  $70^\circ$  are the contact angles of our hydrophobized silica particles at the water/SBO and water/C16 interfaces, respectively; see Section 3.1.

The computational procedure yields also the capillary-bridge force, the shear response force and the maximal value of the latter force, which is related to the yield stress; see Eq. (30). The dimensionless capillary-bridge force, is an universal function that depends on three parameters,  $f = f(\tilde{h}, \Phi, \alpha)$ . Here,  $\tilde{h} = h/(2a)$  is the dimensionless surface-to-surface distance between the two particles; as before,  $a$  is the particle radius and  $\Phi = V_i / V_p$  is the dimensionless bridge volume; see Fig. 11a.

Fig. 12a shows theoretical curves  $f$  vs.  $\Phi$  for pendular rings ( $\tilde{h} = 0$ ) and for various values of  $\alpha$ . Physically, each curve shows the variation of capillary force upon increasing the volume of the liquid bridge at

fixed contact angle,  $\alpha$ . At  $\Phi \rightarrow 0$ , we have  $f \approx \cos \alpha$ , as established by Willett et al. [69]. With the rise of  $\Phi$ , the dimensionless capillary force  $f$  markedly *decreases*. Having in mind that  $S_{\text{oil}} \propto \Phi$ , see Eq. (33), it may seem that the last result is in contradiction with the experimental fact that the yield stress  $Y$  *increases* with the rise of  $S_{\text{oil}}$  (see Figs 8 and 9). Note, however, that  $Y$  is proportional to  $f_{\max} = \max(f_{\text{sh}})$ , rather than to  $f$ , see Eq. (30). In turns,  $f_{\max}$  (unlike  $f$ ) increases with the rise of  $\Phi$ ; see below.

Figs. S4a and b in Appendix B show theoretical curves  $f$  vs.  $\tilde{h}$  for various values of  $\Phi$  and for two fixed contact angles,  $\alpha = 12^\circ$  and  $70^\circ$ . At  $\alpha = 12^\circ$ ,  $f$  monotonically decreases with the rise of  $\tilde{h}$ , i.e. with the bridge extension. In contrast, at  $\alpha = 70^\circ$ ,  $f$  exhibits a non-monotonic dependence on  $\tilde{h}$ , with a maximum. For both contact angles,  $f$  decreases with the rise of  $\Phi$  for the smaller  $\tilde{h}$  (the tendency in Fig. 12a), whereas  $f$  increases with the rise of  $\Phi$  for the greater  $\tilde{h}$  (the opposite tendency).

Upon shear deformation characterized by the angle  $\gamma$  (Fig. 10), the length of the bridge  $h$  increases. These two quantities ( $\gamma$  and  $h$ ) are related (see Appendix A):

$$\tan \gamma = \left[ (\tilde{h} + 1)^2 - 1 \right]^{1/2}; \quad \tilde{h} = h/(2a) \quad (34)$$

The dimensionless force of rheological response upon shear deformation is an universal function,  $f_{\text{sh}} = f_{\text{sh}}(\gamma, \Phi, \alpha)$ . Theoretical curves for  $f_{\text{sh}}$  vs.  $\gamma$  at various values of the dimensionless bridge volume  $\Phi$  and at two fixed contact angles,  $\alpha = 12^\circ$  and  $70^\circ$ , are shown in Figs 12b and c, respectively. Each of these curves has a rightmost endpoint, corresponding to a certain value of  $\gamma$ . For greater values of  $\gamma$  (or  $h$ ), the system of equations in Appendix A has no solution, because either the limitation  $r_0 > 0$  is violated, or the dimensionless volume of the liquid in the bridge becomes greater than the given value of  $\Phi$ ; see Fig. 11a.

The dashed portions of the curves in Fig. 12c correspond to bridge profiles with inflection points, which could be sources of instability [73,74]. Note however, that the maxima of the  $f_{\text{sh}}$ -vs.- $\gamma$  curves in this figure are in the region of profiles without inflection points. In other words, the yield stress  $Y$  is not related to the presence of inflection point on the drop profile. (The bridge profiles corresponding to the curves in Fig. 12b do not have inflection points at all.)

In Fig. 12d we have plotted the maxima of the  $f_{\text{sh}}$  vs.  $\gamma$  curves, like those in Figs. 12b and c, vs. the dimensionless bridge volume,  $\Phi$ , for various values of the contact angle  $\alpha$ . In general,  $f_{\max} = f_{\max}(\Phi, \alpha)$  is an universal function, which determines the yield stress, see Eq. (30), and will be used to fit the experimental data (Section 5). For this reason, the function  $f_{\max}(\Phi, \alpha)$  is tabulated in Appendix C, Table C1. This table can be used as a database for computation of  $f_{\max}(\Phi, \alpha)$  by using a four-point interpolation formula, as explained in Appendix C. For fast estimates of  $f_{\max}(\Phi, \alpha)$ , one can use the approximate equation (of accuracy better than 0.6%):

$$f_{\max}(\Phi, \alpha) \approx (0.1763 + 0.0912\varphi + 0.0165\varphi^2) \cos \alpha \quad \text{for } \alpha \leq \alpha_0 \quad (35)$$

$$\alpha_0 (\text{deg}) = 51.5 - 19.5\varphi - 2.5\varphi^2, \quad \varphi = \log_{10} \Phi (\%)$$

$0.01\% \leq \Phi \leq 10\%$ ;  $\Phi$  is related to  $S_i$  by Eq. (33); see Fig. S7b and Table B1 in Appendix B. The substitution of Eq. (35) into Eq. (30) gives an approximate analytical formula for estimating the yield stress,  $Y$ .

The theoretical curves in Fig. 12d show that  $f_{\max}$  increases with the rise of  $\Phi$ , in agreement with the tendency of the experimental curves in Figs. 8 and 9. For  $\alpha < 20^\circ$ ,  $f_{\max}$  weakly depends on the contact angle,  $\alpha$ . However, for  $\alpha > 20^\circ$ ,  $f_{\max}$  markedly decreases with the rise of  $\alpha$  and becomes about three times smaller at  $\alpha = 70^\circ$ ; see also Fig. S7a in Appendix B, which shows the dependence of  $f_{\max}$  on  $\alpha$  at fixed  $\Phi$ . Fig. S7b compares the approximate Eq. (35) with the exact function  $f_{\max}(\Phi, \alpha)$ . At not too high values of  $\Phi$  and  $\alpha$ , in view of Eqs. (30) and

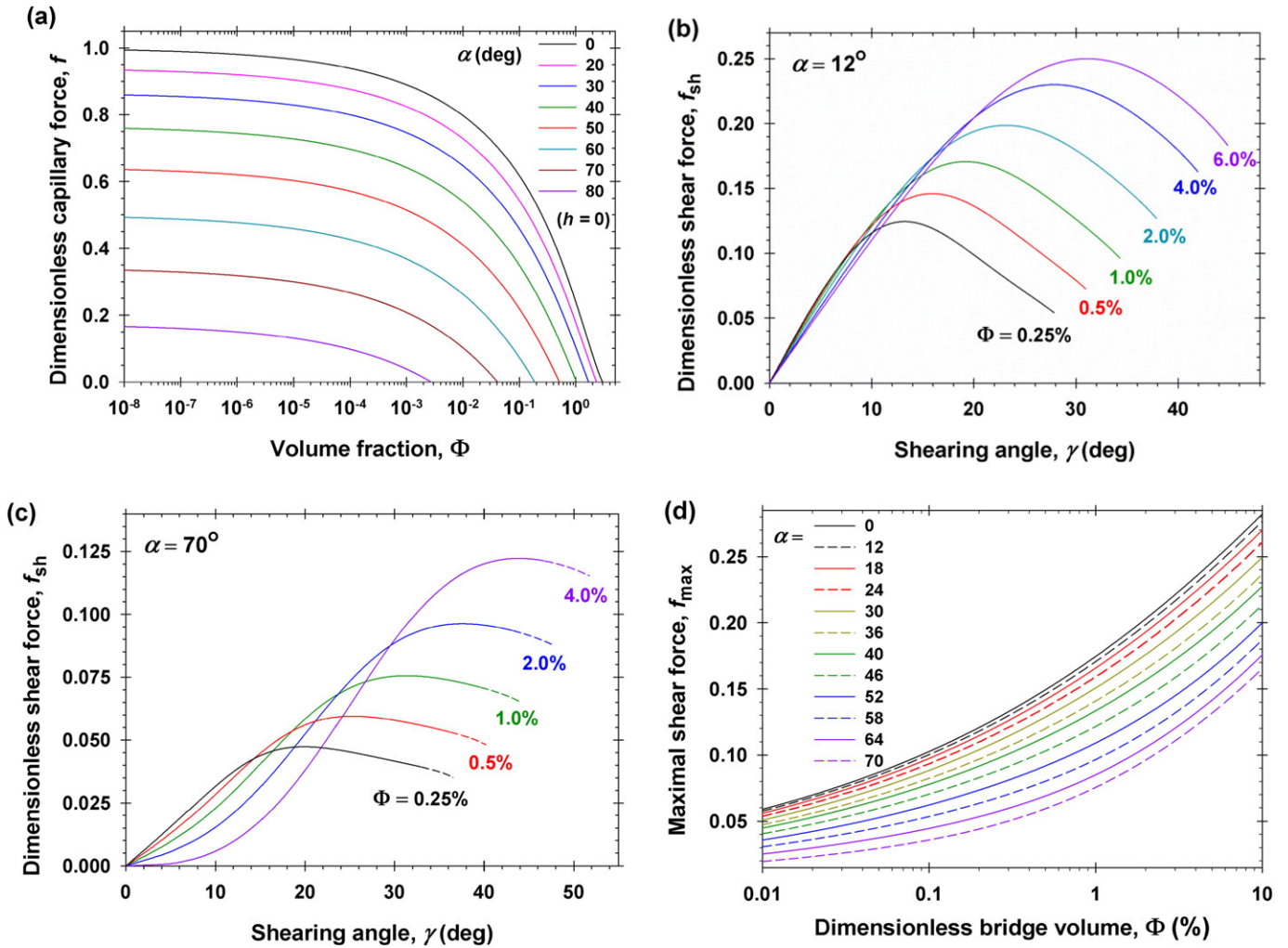


**Fig. 12.** Theoretical dependences calculated by using the exact capillary bridge theory. (a) The dimensionless capillary-bridge force,  $f = F_{\text{cap}}/(2\pi a\sigma)$ , vs. the dimensionless bridge volume,  $\Phi$ , for  $h = 0$  (pendular rings) and different values of contact angle,  $\alpha$ . (b) The dimensionless force of shear response,  $f_{\text{sh}} = f_{\text{cap}}\sin\gamma$ , vs. the shearing angle,  $\gamma$ , at  $\alpha = 12^\circ$  for different  $\Phi$  values. (c)  $f_{\text{sh}}$  vs.  $\gamma$  at  $\alpha = 70^\circ$  for different  $\Phi$ ; the dashed portions of the curves correspond to bridges with inflection points. (d) Plot of the maximal value of  $f_{\text{sh}}$ , denoted  $f_{\text{max}}$ , vs.  $\Phi$  for different contact angles,  $\alpha$ .

(35) we have  $Y \propto f_0(\Phi)\cos\alpha$ , as stated in the empirical expressions for  $Y$  cited in the literature [3,9,14,16,25]; Eq. (35) gives the explicit form of  $f_0(\Phi)$ .

To verify whether neighboring capillary bridges could overlap during the shear deformation, as an example let us consider the simple cubic lattice with 6 bridges per particle shown in Fig. 10.

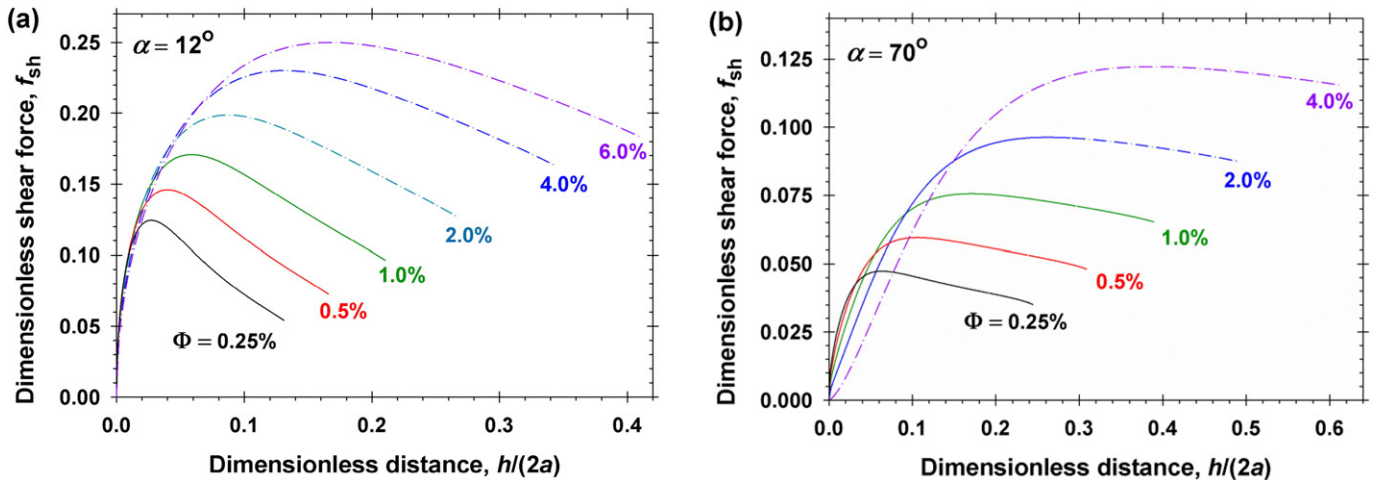


**Fig. 13.** The calculated dimensionless force of shear response,  $f_{\text{sh}}$ , vs. the dimensionless length of the bridge,  $\bar{h} = h/(2a)$ , for different  $\Phi$  values: (a)  $\alpha = 12^\circ$ ; (b)  $\alpha = 70^\circ$ . Six bridges per particle have been assumed. The dash-dotted lines correspond to overlap of the bridges on the particle surface.

Two neighboring bridges will not overlap if the following relation is satisfied:

$$\gamma + \varphi_c(h) + \varphi_c(0) < \frac{\pi}{2} \quad (36)$$

see Figs. 10b and 11a. The central angles  $\varphi_c(h)$  and  $\varphi_c(0)$  are calculated in the course of the computational procedure (see Appendix A). Fig. 13 shows plots of  $f_{sh}$  vs.  $\tilde{h}$  for various fixed values of  $\Phi$  at two contact angles:  $\alpha = 12^\circ$  and  $70^\circ$ . The portions of the curves that are shown with dash-dotted lines correspond to shear deformations, for which the relation in Eq. (36) is violated, so that the two neighboring bridges overlap. In Fig. 13a ( $\alpha = 12^\circ$ ), for  $\Phi = 2\%$ ,  $4\%$  and  $6\%$  the maxima of the curves belong to the overlap zone, whereas in Fig. 13b ( $\alpha = 70^\circ$ ) only the curve with  $\Phi = 4\%$  belongs to the overlap zone. In the case of overlap, the system undergoes a transition from pendular to funicular state, and the theoretical dependences calculated assuming pendular state are not valid. The data presented in Fig. 13 indicate that a transition from pendular to funicular state is possible in the investigated suspensions upon shear deformations. Hence, such a transition is a possible reason for the deviations of the points from the theoretical lines in Figs. 8 and 9 at the greatest  $S_{oil}$  values.

## 5. Theoretical interpretation of rheological data

### 5.1. The experimental yield stress

The rotational rheometer measures the moment of force (torque)  $M$  acting on the rotating disk; see Fig. 7a:

$$M = 2\pi \int_0^R \tau_{z\varphi} \rho^2 d\rho \quad (37)$$

Here,  $(\rho, \varphi, z)$  are cylindrical coordinates with  $z$ -axis directed along the rheometer's axis of rotation, and  $\tau_{z\varphi}$  is the respective component of the stress tensor, which acts tangentially to the rotating disk. The mean value of the stress is defined as follows:

$$\tau = \frac{3}{R^3} \int_0^R \tau_{z\varphi} \rho^2 d\rho = \frac{3M}{2\pi R^3} \quad (38)$$

The above relation is programmed in the rheometer to compute  $\tau$  from the experimentally measured  $M$ . If  $\tau_{z\varphi}$  was constant, from Eq. (38) one would obtain  $\tau = \tau_{z\varphi}$ . The experimental yield stress  $Y$  is identified with the value of  $\tau$  at the kink of the experimental dependence of  $\psi$  vs.  $\tau$ ; see Fig. 7b.

### 5.2. Models of the deformation zone

As seen in Fig. 7b, the experimental values of  $\psi$  at the kinks vary in the range  $\psi_Y = 0.01$ – $0.1$  (rad), that is  $\psi_Y = 0.57^\circ$  –  $5.7^\circ$ . In contrast, in Fig. 12b the values of the shearing angles corresponding to the maxima are considerably larger, in the range  $\gamma = 13^\circ$  –  $31^\circ$ . The possible explanation of this difference is that the deformation of the suspension at  $\tau = Y$  happens only in a certain zone adjacent to the mobile disk, while the rest of suspension remains immobile; see e.g. Fig. 14a. Similar fluidization in the vicinity of a rotating disk was observed by Buttinoni et al. in model experiments with ordered monolayers of colloidal particles at liquid interfaces for both steady [84] and oscillatory [85] rotation. Depending on the shape of the deformation zone, at least two models are possible, as follows.

**Model A: Plane-parallel zone of deformation.** In this case, it is assumed that the shape of the deformation zone is induced by the geometry of the experimental setup, viz. two parallel plates. The zone of deformation is a

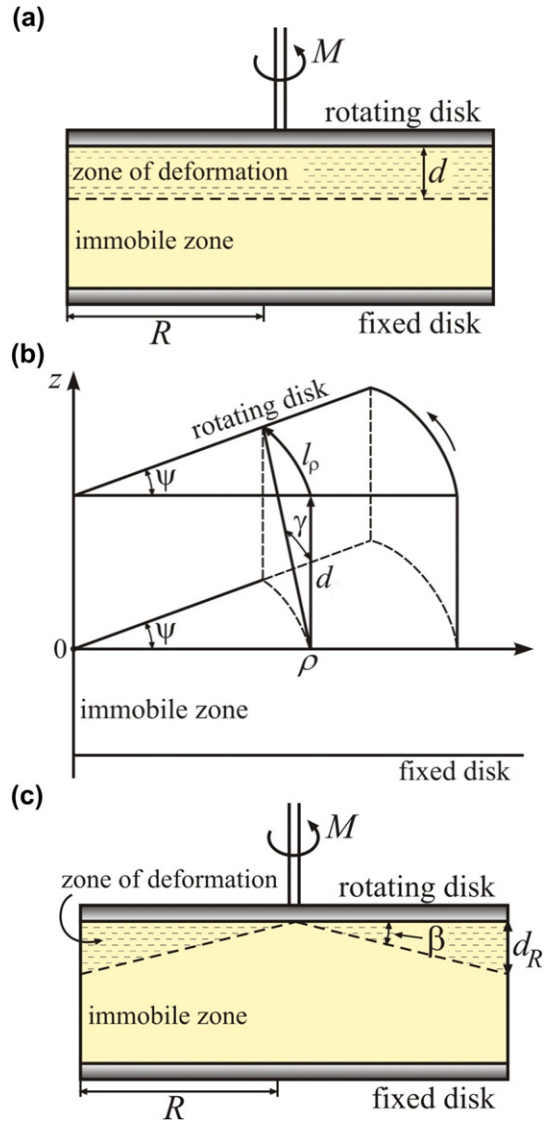


**Fig. 14.** (a) Sketch of a plane-parallel zone of deformation near the upper rotating disk of the rheometer; the shear strain is zero in the immobile zone. (b) Relation between the rotation angle  $\psi$  and the shearing angle,  $\gamma$ , for the uppermost layer of the suspension;  $l_\rho$  is the displacement and  $d_\rho$  is the thickness of the zone of deformation. (c) Sketch of a conical zone of deformation.

planar layer of thickness  $d$  adjacent to the mobile disk of the rheometer; see Fig. 14a. In such a case, the local displacement of the particles in the uppermost layer of the suspension (supposedly attached to the rotating disk) is

$$l_\rho = 2\rho \sin \frac{\psi}{2} \quad (39)$$

Then, the true shearing angle,  $\gamma$ , is given by the equation (see Fig. 14b):

$$\tan \gamma = \frac{l_\rho}{d} = \frac{2\rho}{d} \sin \frac{\psi}{2} \quad (40)$$

Note that at given  $\psi$ , the displacement angle  $\gamma$  depends on the radial distance  $\rho$ . Next, in view of Eqs. (27)–(29) and (38) the experimental yield stress is determined by the expression:

$$Y = \frac{2\sigma}{a} c_g \phi_p^{2/3} \max(G), \quad G \equiv \frac{3}{R^3} \int_0^R f_{sh}(\gamma) \rho^2 d\rho \quad (41)$$

where  $R$  is the radius of the rheometer's disk, and the relation “max” is with respect to the rotation angle  $\psi$ . Using the substitution  $y = (2\rho/d)\sin(\psi/2)$ , along with Eq. (40), we bring the last integral in the form:

$$G(u) = \frac{3}{u^3} \int_0^u f_{sh}(\arctan(y)) y^2 dy, \quad u \equiv \frac{2R}{d} \sin \frac{\psi}{2} \quad (42)$$

$G(u)$  is a universal function of  $u$ . It can be calculated by integrating the theoretical curves for  $f_{sh}(\gamma)$ , like those in Fig. 12b and c, with  $\gamma = \arctan(y)$ . The calculations show that the function  $G(u)$  has a maximum,  $G_{max}$ , corresponding to a certain value  $u = u_{max}$ . Then, the yield stress,  $Y$ , is determined by Eq. (41) with  $\max(G) = G_{max}$  and, in view of Eq. (42) the yield strain can be found from the expression:

$$\sin \frac{\psi_Y}{2} = \frac{d}{2R} u_{max} \quad (43)$$

$G(u)$  defined by the integral in Eq. (42) is a universal function of  $u$ , where the function  $f_{sh}$  is to be calculated for a pair of particles connected with a capillary bridge as explained in Appendix A. For this reason, the height of the maximum,  $G_{max}$ , and the position of the maximum,  $u_{max}$ , are independent of the thickness of the deformation zone,  $d$  (see Fig. 14a). Hence, in view of Eq. (41) the yield stress is independent of  $d$  and represents a characteristic of the elastic limit of the investigated capillary suspension. In contrast, the yield strain  $\psi_Y$  depends on  $d$ ; see Eq. (43). Dependencies of  $G_{max}$  on  $\Phi$  calculated for various values of the contact angle  $\alpha$  are shown in Fig. S6 in Appendix B. Qualitatively, these dependences resemble the curves for  $f_{max}$  in Fig. 12d.

**Model B: Conical zone of deformation.** In reality, the border between the zone of deformation and the immobile zone is spontaneously established in the course of deformation. In such a case, at  $\psi = \psi_Y$  mobile would be those particles, for which the applied shear force is  $> f_{max}$ , and immobile would be the particles, for which  $f_{sh} < f_{max}$ ; see Fig. 11b. Hence, we have  $f_{sh} = f_{max}$  at the border of the deformation zone. Here, we will prove that in this case the border has a conical shape, as shown in Fig. 14c.

For a conical border, the thickness of the zone of deformation,  $d(\rho)$ , increases proportionally to the radial coordinate  $\rho$ :

$$d(\rho) = \rho \tan \beta \quad (44)$$

where  $\beta = \text{const.}$  is the angle of the cone in Fig. 14. Then, in view of Eq. (40) we obtain

$$\tan \gamma = \frac{2\rho}{d(\rho)} \sin \frac{\psi}{2} = \frac{2 \sin(\psi/2)}{\tan \beta} = \text{const.} \quad (45)$$

i.e. the right-hand side of Eq. (45) is independent of  $\rho$ . Then,  $\gamma$  is also independent of  $\rho$  and from Eq. (41) we derive:

$$\begin{aligned} \max(G) &= \max \left[ \frac{3}{R^3} \int_0^R f_{sh}(\gamma) \rho^2 d\rho \right] \\ &= \max \left[ f_{sh}(\gamma) \frac{3}{R^3} \int_0^R \rho^2 d\rho \right] = \max[f_{sh}(\gamma)] = f_{max} \end{aligned} \quad (46)$$

see, e.g., Figs. 12 b and c. Consequently, for a conical border of the deformation zone, Eq. (41) becomes identical with Eq. (30). The maximal force  $f_{max}$  characterizes the interaction between two particles connected by a capillary bridge. Consequently,  $f_{max}$  is independent of the cone angle  $\beta$ . Hence, in view of Eq. (30) the yields stress  $Y$  is also independent of the shape of the deformation zone characterized by  $\beta$ . In other words,  $Y$  characterizes the elastic limit of the investigated

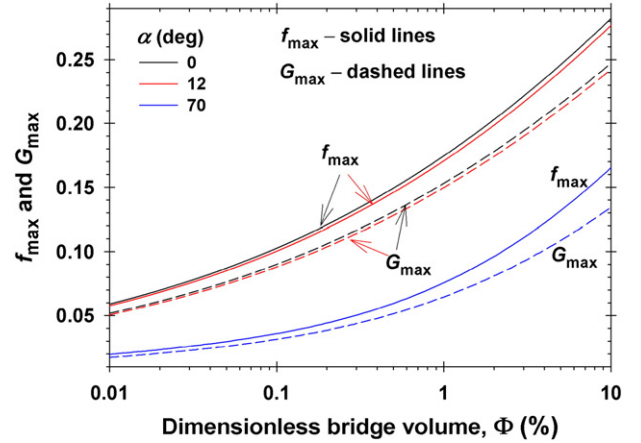


Fig. 15. Theoretical dependences of  $f_{max}$  (conical deformation zone) and  $G_{max}$  (plane-parallel deformation zone) on the dimensionless bridge volume,  $\Phi$ , for three different values of the contact angle,  $\alpha$ .

capillary suspension. In contrast, in view of Eq. (45) the yield strain  $\psi_Y$  depends on  $\beta$ :

$$\sin \frac{\psi_Y}{2} = \frac{1}{2} (\tan \beta) \tan \gamma_Y \quad (47)$$

The cone angle is expected to be relatively small,  $\tan \beta < 1$  (Fig. 14c). Then, Eq. (47) provides an explanation of the fact that the experimental rotation angle  $\psi_Y$  (Fig. 7b) is essentially smaller than the theoretical yield strain  $\gamma_Y$ , corresponding to the maxima of the curves in Fig. 12b.

**Comparison of the two models.** Fig. 15 compares plots of  $G_{max}$  vs.  $\Phi$  and  $f_{max}$  vs.  $\Phi$  at three values of the three-phase contact angle,  $\alpha = 0, 12^\circ$  and  $70^\circ$ . The calculated curves show that  $f_{max}$  is greater than  $G_{max}$ , but the difference between these two quantities is not so considerable. In other words, the experimental data could be fitted by both models A and B (Fig. 14a and c) by varying the geometrical coefficient  $c_g$  in Eqs. (30) and (41). Because in reality the border between the zone of deformation and the immobile zone is established spontaneously in the course of deformation, we believe that model B is more realistic. Correspondingly, the theoretical curves in Figs. 8 and 9 have been drawn by using the model B.

### 5.3. Theory vs. experiment and discussion

To illustrate the magnitudes and ranges of variation of the system's parameters, in Table 2 we compare their values for two of the experimental curves in Fig. 7b corresponding to  $S_{oil} = 0.72\%$  and  $2.68\%$  for bridges from SBO in water. For both suspensions, the contact angle is  $\alpha = 12^\circ$ ; the particle radius is  $a = 1.9 \mu\text{m}$  and the particle volume fraction is  $\phi_p = 40\%$  and the mean number of bridges per particle is  $n = 4.67$ ; see Eq. (2). The values of  $\Phi$  calculated from Eq. (33) are smaller than those of  $S_{oil}$  (Table 2) The values of the shearing angle at the elastic limit,  $\gamma_Y$ , correspond to the maxima of the respective

Table 2  
Comparison of parameter values for two of the experimental curves in Fig. 7b.

Parameter	$S_{oil} = 0.72\%$	$S_{oil} = 2.68\%$
$\Phi$ (%)	0.2314	0.8613
$h_Y/(2a)$	0.0262	0.0540
$\gamma_Y$ (°)	12.97	18.41
$\psi_Y$ (°)	1.278	0.756
$\beta$ (°)	5.531	2.270
$l_R$ (mm)	0.446	0.264
$d_R$ (mm)	1.937	0.793
$N_R$	510	209

theoretical curves, like those in Fig. 12b. The dimensionless surface-to-surface distance between two particles,  $\hat{h}_Y = h_Y / (2a)$ , which characterizes the length of the bridge at the elastic limit, is related with  $\gamma_Y$  by Eq. (34). As seen in Table 2,  $h_Y$  is small (2.6%–5.4%) in comparison with the particle diameter  $2a$ .

The values of the rotation angle at the elastic limit,  $\psi_Y$ , are determined from the experimental curves in Fig. 7b. As seen in Table 2, we have  $\psi_Y \ll \gamma_Y$ . Such a difference between the apparent and actual strain implies that only a part of the suspension is subjected to deformation; see Fig. 14.

Furthermore, adopting the model with conical deformation zone (model B; Fig. 14c), from the values of  $\psi_Y$  and  $\gamma_Y$  we estimate the cone angle  $\beta$  using Eq. (47). As seen in Table 2,  $\beta$  is greater for the softer suspension with smaller content of inner phase,  $S_{oil} = 0.72\%$ . The displacement at the disk periphery,  $l_R$ , is calculated from Eq. (39) with  $\rho = R$  and  $\psi = \psi_Y$ . The thickness of the deformation zone at the disk periphery,  $d_R = d(R)$  is calculated from Eq. (44). For the softer suspension with  $S_{oil} = 0.72\%$  the value of  $d_R$  is only slightly smaller than the distance between the two disks of the rheometer (the gap distance), which has been 2 mm in our experiments. The last row in Table 2 gives the number of particle layers in the zone of deformation at the disk periphery estimated as  $N_R = d_R / (2a)$ , where  $2a = 3.8 \mu\text{m}$  is the mean particle diameter. The obtained values  $N_R = 510$  and 209 mean that the deformation zone contains a considerable number of particle layers, so that the capillary suspension can be treated as a continuous medium.

The theoretical curves in Figs. 8 and 9 are drawn in accordance with Eq. (30) using the experimental values of  $\sigma$ ,  $a$ ,  $\phi_p$  and  $\alpha$ , and the computational procedure from Appendix A. The values on the mean number of bridges per particle,  $n$ , given in these figures are estimated from Eq. (2). Good agreement was achieved by varying only a single adjustable parameter,  $c_g$ . To compare the magnitudes of the yield stress  $Y$  for the suspensions with capillary bridges from C16 and SBO, in Fig. 16a we have collected the best fits from Figs. 8, 9, and S8 (the latter in Appendix B). One sees that at the same particle volume fraction,  $\phi_p$ , the yield stress is higher for the suspensions with SBO. This result might seem surprising because the water/C16 interfacial tension is 52 mN/m vs. only 30 mN/m for water/SBO. However, in this case the effect of contact-angle difference ( $70^\circ$  vs.  $12^\circ$ ) is stronger and predominant, and leads to lower  $f_{max}$  and yield stress  $Y$ , for the suspension with higher contact angle  $\alpha$ ; see Eq. (30) and Fig. S7a in Appendix B.

As already mentioned, the geometrical coefficient  $c_g$  was determined as an adjustable parameter from the fits. In Fig. S9, it is illustrated how the variation of  $c_g$  influences the comparison theory – experiment. In Fig. 16b, the values of  $c_g$  are plotted vs.  $\phi_p$  for all studied systems. In the case of SBO bridges,  $c_g$  increases linearly with  $\phi_p$ . In the case of C16 bridges,  $c_g$  is smaller than that for SBO bridges at the smaller  $\phi_p$ , but increases exponentially at the higher  $\phi_p$  values. The parameters of the respective fits with empirical curves are shown in Fig. 16b.

The obtained  $c_g$ -vs.- $\phi_p$  dependencies call for discussion. Our theoretical model (where  $c_g$  is a purely geometrical parameter) corresponds to an idealized situation that can be summarized as follows:

- (i) The *whole* amount of the inner liquid phase is split to capillary bridges of identical volumes formed around *all* contact points of neighboring particles.
- (ii) The solid particles are *uniformly* distributed in the outer liquid phase.
- (iii) The capillary bridges, connecting a given particle with neighboring particles, *do not overlap* on the particle surface.

Of course, deviations from the above idealized picture are possible because the dispersing of the bridge phase to small drops and their transformation to liquid bridges between neighboring particles is a dynamic process dependent on many factors, so that its result could be different from the above idealized picture. In particular, the number of closest neighbors of a given particle (the coordination number),  $n$ ,

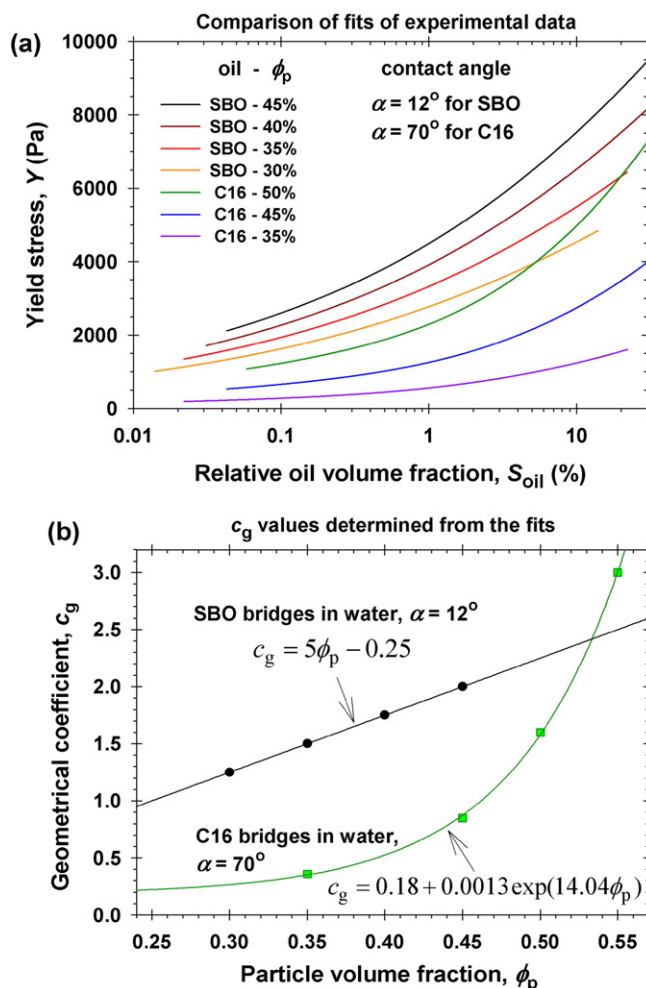


Fig. 16. (a) Comparison of the fits of experimental data for the yield stress,  $Y$  vs.  $S_{oil}$ , for SBO and C16 capillary bridges in water. (b) Plots of the geometrical coefficient,  $c_g$ , vs. the particle volume fraction,  $\phi_p$ , determined from the fits;  $\alpha$  is the contact angle across the bridge (oil) phase.

could be greater than the number of capillary bridges per particle,  $m$ , i.e.  $n \geq m$ .

For example, in the case of bridges from C16 a competition of two factors acting in the opposite directions takes place. First, the relatively high value of the three-phase contact angle,  $\alpha = 70^\circ$  (vs.  $\alpha = 12^\circ$  in the case of SBO), is related to a lower gain of surface energy upon attachment of an oil droplet (a potential capillary bridge) to the particle surface. In other words, the formation of capillary bridges is energetically less favorable in the case of C16 as compared to SBO. Consequently, it might happen that not all possible capillary bridges from C16 are formed, and this might explain the smaller values of  $c_g$  at the lower  $\phi_p$  in Fig. 16b.

Second, C16 has a considerably lower viscosity than SBO,  $\eta = 3.0$  vs. 50 (mPa·s). At a given  $S_{oil}$ , this leads to the formation of a greater number of smaller emulsion drops in the case of SBO [86]. This effect is strengthened at the greater  $\phi_p$ , insofar as the higher particle volume fractions lead to a higher effective viscosity of the outer liquid phase [87,88]. The higher concentration of emulsion droplets raises the probability for bridge formation during the stirring of the dispersion. This effect could explain the significant increase of  $c_g$  at the higher  $\phi_p$  values (Fig. 16b).

Another issue that deserves discussion is the effect of particle polydispersity. In some two-dimensional systems, the capillary forces could lead to separation of the bigger particles from the smaller ones [89]. However, this is unlikely to happen in the investigated capillary

suspensions, because the dispersion is initially subjected to intensive stirring, and then it quickly solidifies. This leads to random spatial distribution of particles of different sizes. One could expect that the yield stress in a suspension with moderately polydisperse particles is close to the yield stress in a suspension of monodisperse particles of diameter equal to the mean diameter of the polydisperse particles. Similar behavior has been observed with monolayers from charged colloid particles: the surface pressure vs area isotherms obey the same power law for monodisperse and polydisperse particles [79].

Contact angle *hysteresis* is usually present at solid surfaces, the absence of hysteresis being exclusion [90–93]. Hysteresis is present not only at rough and heterogeneous surfaces, but also at smooth and homogeneous surfaces [90,93]. For contact angles in the range  $0^\circ < \alpha < 30^\circ$ , the dependence of the yield stress,  $Y$ , on angle  $\alpha$  (and its hysteresis) is expected to be weak; however, for  $30^\circ < \alpha < 90^\circ$  this dependence could be stronger; see Fig. 12d. Because the yield stress is related to the bridge extension, a better agreement between theory and experiment is expected if  $\alpha$  is identified with the receding angle with respect to the bridge phase.

## 6. Conclusions

Suspensions of hydrophobic particles in water or hydrophilic particles in oil possess the remarkable property to solidify upon the addition of minimal amount of a second liquid that preferentially wets the particles. The hardening is due to the formation of capillary bridges (pendular rings), which connect the particles. Here, we reviewed works on the mechanical properties of such suspensions and related works on the capillary-bridge force, and presented new rheological data for the weakly studied concentration range 30–55 vol% particles. These capillary suspensions exhibit quasi-elastic behavior when subjected to small shear deformations (Fig. 7). Their mechanical strength, characterized by the yield stress  $Y$ , was measured at the elastic limit for various volume fractions of the particles and of the preferentially wetting liquid. In addition, a quantitative theoretical model was developed, which relates  $Y$  with the maximum of the capillary-bridge force, projected on the shear plane (Fig. 11b). A semi-empirical expression for the dependence of the number of closest neighbors,  $n$ , on the particle volume fraction,  $\phi_p$ , was established and applied to estimate the mean number of capillary bridges per particle; see Eq. (2) and Fig. 3.

The model agrees very well with the experimental data (Figs. 8 and 9) and gives a quantitative description of the yield stress  $Y$ , which increases with the rise of interfacial tension,  $\sigma$ , and with the volume fractions of particles,  $\phi_p$ , and capillary bridges,  $\Phi$ , but decreases with the rise of particle radius,  $a$ , and contact angle  $\alpha$ ; see Eq. (30). In particular, the shear stress is proportional to the projection of capillary force on the shear plane,  $F_{\text{cap}} \sin \gamma$ , where  $\gamma$  is the shearing angle. The capillary force decreases with the bridge extension (with the rise of  $\gamma$ ), whereas  $\sin \gamma$  increases, so that their product,  $F_{\text{cap}} \sin \gamma$ , has a *maximum* value at a certain strain  $\gamma = \gamma_Y$ , which determines the limit of the elastic response of the system, that is the yield stress,  $Y$ . The calculation of  $F_{\text{cap}}$  for the extended bridge is based on the exact theory and numerical calculation of the capillary bridge profile at various bridge volumes and contact angles. For easier computation of the yield stress, the numerical results are presented as a database in Appendix C. An approximate analytical formula for  $Y$  is also derived; see Eq. (35).

The comparison of the theoretical and experimental strain at the elastic limit reveals that the fluidization of the capillary suspension takes place only in a deformation zone of thickness up to several hundred particle diameters, which is adjacent to the mobile plate of the rheometer (Fig. 14 and Table 2). The experimental results reported in this article refer to water-continuous suspension with hydrophobic particles and oily capillary bridges. The comparison of data for bridges from soybean oil (SBO) and hexadecane (C16) surprisingly indicate that the yield strength is greater for the suspension with SBO despite its lower interfacial tension against water. The result can be explained with the

different contact angles of the two oils in agreement with the theoretical predictions. In a subsequent study, we plan to extend the present analysis to the inverse system, viz. oil-continuous suspension with hydrophilic particles and aqueous capillary bridges.

We hope that the results reported here will contribute for a better understanding, quantitative prediction and control of the mechanical properties of three-phase capillary suspensions particles/oil/water, or more generally, solid/liquid/liquid.

## Acknowledgements

The authors gratefully acknowledge the support from Unilever R&D and from the Horizon 2020 project ID: 692146-H2020-eu.4.b “Materials Networking”. The authors are grateful to Dr. Sylvia Tzocheva, Ms. Denitsa Krusteva and Dr. Plamen Petkov for their contributions to the experiments, and to Mrs. Mariana Paraskova for her assistance in figure preparation.

## Appendices A, B and C. Supplementary data

Appendix A “System of equations and computational procedure”; Appendix B “Additional experimental and computational results”, and Appendix C “Database and interpolation formula for calculating the yield stress”, are presented as Supplementary material associated with this article, which can be found in the online version, at <https://doi.org/10.1016/j.cis.2017.11.004>. Therein, the reader could find the tabulated function  $f_{\text{max}}(\Phi, \alpha)$ , which is appended as an electronic Excel file.

## References

- [1] Koos E, Willenbacher N. Capillary forces in suspension rheology. *Science* 2011;331:897–900.
- [2] McCullor J, Himes P, Anklaam MR. The effects of capillary forces on the flow properties of glass particle suspensions in mineral oil. *AIChE J* 2011;57:2334–40.
- [3] Bossler F, Weyrauch L, Schmidt R, Koos E. Influence of mixing conditions on the rheological properties and structure of capillary suspensions. *Colloids Surf A* 2017;518:85–97.
- [4] Rumpf H, Schubert H. The behavior of agglomerates under tensile strain. *J Chem Engineering Japan* 1974;7:294–8.
- [5] Schubert H. Capillary force-modeling and application in particulate technology. *Powder Technol* 1984;37:105–16.
- [6] Koos E. Capillary suspensions: particle networks formed through the capillary force. *Curr Opin Colloid Interface Sci* 2014;19:575–84.
- [7] Domenech T, Velankar SS. On the rheology of pendular gels and morphological developments in paste-like ternary systems based on capillary attraction. *Soft Matter* 2015;11:1500–16.
- [8] Velankar SSA. non-equilibrium state diagram for liquid/fluid/particle mixtures. *Soft Matter* 2015;11:8393–403.
- [9] Bossler F, Koos E. Structure of particle networks in capillary suspensions with wetting and nonwetting fluids. *Langmuir* 2016;32:1489–501.
- [10] Mitarai N, Nori F. Wet granular materials. *Adv Phys* 2006;55:1–45.
- [11] Strauch S, Herminghaus S. Wet granular matter: a truly complex fluid. *Soft Matter* 2012;8:8271–80.
- [12] Orr FM, Scriven LE, Rivas AP. Pendular rings between solids: meniscus properties and capillary force. *J Fluid Mech* 1975;67:723–42.
- [13] Koos E, Willenbacher N. Particle configurations and gelation in capillary suspensions. *Soft Matter* 2012;8:3988–94.
- [14] Koos E, Johannsmeier J, Schwebler L, Willenbacher N. Tuning suspension rheology using capillary forces. *Soft Matter* 2012;8:6620–8.
- [15] Koos E, Kannowade W, Willenbacher N. Restructuring and aging in a capillary suspension. *Rheol Acta* 2014;53:947–57.
- [16] Hoffmann S, Koos E, Willenbacher N. Using capillary bridges to tune stability and flow behavior of food suspensions. *Food Hydrocoll* 2014;40:44–52.
- [17] Wollgarten S, Yuce C, Koos E, Willenbacher N. Tailoring flow behavior and texture of water based cocoa suspensions. *Food Hydrocoll* 2016;52:167–74.
- [18] Bitsch B, Dittmann J, Schmitt M, Scharfer P, Schabel W, Willenbacher NA. Novel slurry concept for the fabrication of lithium-ion battery electrodes with beneficial properties. *J Power Sources* 2014;265:81–90.
- [19] Schneider M, Koos E, Willenbacher N. Highly conductive, printable pastes from capillary suspensions. *Sci Rep* 2016;6:31367.
- [20] Bitsch B, Gallasch T, Schroeder M, Börner M, Winter M, Willenbacher N. Capillary suspensions as beneficial formulation concept for high energy density Li-ion battery electrodes. *J Power Sources* 2016;328:114–23.
- [21] Jampolski L, Sanger A, Jakobs T, Guthausen G, Kolb T, Willenbacher N. Improving the process ability of coke water slurries for entrained flow gasification. *Fuel* 2016;185:102–11.



- [22] Dapeng W, Wang X, Yuan Y, Li W, Tian H, Zhao S. Increasing the apparent shear viscosity of polymer composites by uptake of a small amount of water. *RSC Adv* 2014;4:24686–91.
- [23] Domenech T, Velankar S. Capillary-driven percolating networks in ternary blends of immiscible polymers and silica particles. *Rheol Acta* 2014;53:593–605.
- [24] Heidlebaugh S, Domenech T, Iasella S, Velankar SS. Aggregation and separation in ternary particle/oil/water systems with fully-wettable particles. *Langmuir* 2014;30:63–74.
- [25] Dittmann J, Koos E, Willenbacher N. Ceramic capillary suspensions: novel processing route for macroporous ceramic materials. *J Am Ceram Soc* 2013;96:391–7.
- [26] Dittmann J, Willenbacher N. Micro structural investigations and mechanical properties of macro porous ceramic materials from capillary suspensions. *J Am Ceram Soc* 2014;97:3787–92.
- [27] Maurath J, Dittmann J, Schultz N, Willenbacher N. Fabrication of highly porous glass filters using capillary suspension processing. *Sep Purif Technol* 2015;149:470–8.
- [28] Sun H, Yuen MMF. Conductivity enhancement of thermal interface material via capillary attraction. *IEEE 66th Electronic Components and Technology Conference (ECTC) 2016:1409–14*. <https://doi.org/10.1109/ECTC.2016.94>.
- [29] Goyal A, Hall CK, Velev OD. Phase diagram for stimulus-responsive materials containing dipolar colloidal particles. *Phys Rev E* 2008;77:031401.
- [30] Kim S-H, Yi G-R, Kim KH, Yang S-M. Photocurable pickering emulsion for colloidal particles with structural complexity. *Langmuir* 2008;24:2365–71.
- [31] Stratford K, Adhikari R, Pagonabarraga I, Desplat J-C, Cates ME. Colloidal jamming at interfaces: a route to fluid-bicontinuous gels. *Science* 2005;309:2198–201.
- [32] Herzig EM, White KA, Schofield AB, Poon WCK, Clegg PS. Bicontinuous emulsions stabilized solely by colloidal particles. *Nat Mater* 2007;6:966–71.
- [33] White KA, Schofield AB, Binks BP, Clegg PS. Influence of particle composition and thermal cycling on bijel formation. *J Phys Condens Matter* 2008;20:494223.
- [34] Haase MF, Sharifi-Mood N, Lee D, Stebe KJ. In situ mechanical testing of nanostructured Bijel fibers. *ACS Nano* 2016;10:6338–44.
- [35] Binks BP. Particles as surfactants – similarities and differences. *Curr Opin Colloid Interface Sci* 2002;7:21–41.
- [36] Aveyard R, Binks BP, Clint JH. Emulsions stabilised solely by colloidal particles. *Adv Colloid Interface Sci* 2003;100–102:503–46.
- [37] Golemanov K, Tcholakova S, Kralchevsky PA, Ananthapadmanabhan KP, Lips A. Latex-particle-stabilized emulsions of anti-Bancroft type. *Langmuir* 2006;22:4968–77.
- [38] Donev A, Torquato S, Stillinger FH, Connelly R. Jamming in hard sphere and disk packings. *J Appl Phys* 2004;95:989–99.
- [39] McFarlane JS, Tabor D. Adhesion of solids and the effect of surface films. *Proc R Soc London A* 1950;202:224–43.
- [40] Zimon AD. Adhesion of dust and powder. London: Springer; 1969.
- [41] Haines WB. Studies in the physical properties of soils: II. A note on the cohesion developed by capillary forces in an ideal soil. *J Agric Sci* 1925;15:529–35.
- [42] Fisher RA. On the capillary forces in an ideal soil; correction of formulae given by W. B. Haines. *J Agric Sci* 1926;16:492–505.
- [43] Iveson SM, Lister JD. Liquid-bound granule impact deformation and coefficient of restitution. *Powder Technol* 1998;99:234–42.
- [44] Iveson SM, Lister JD. Fundamental studies of granule consolidation part 2: quantifying the effects of particle and binder properties. *Powder Technol* 1998;99:243–50.
- [45] Carman PC. Properties of capillary-held liquids. *J Phys Chem* 1953;57:56–64.
- [46] Woodrow J, Chilton H, Hawes RI. Forces between slurry particles due to surface tension. *J Nucl Energy B, Reactor Tech* 1961;1:229–37.
- [47] Kingery WD. Densification during sintering in the presence of a liquid phase. I. Theory. *J Appl Phys* 1959;30:301–6.
- [48] Heady RB, Cahn JW. An analysis of the capillary forces in liquid-phase sintering of spherical particles. *Metallurgical Trans* 1970;1:185–9.
- [49] Sheetz DP. Formation of films by drying of latex. *J Polymer Sci* 1965;9:3759–73.
- [50] Vanderhoff JW, Tarkowski HL, Jenkins MC, Bradford EB. Theoretical consideration of interfacial forces involved in coalescence of latex particles. *Rubber chemistry, Dent Tech* 1967;40:1246–9.
- [51] Keddie JL. Film formation of latex. *Materials Sci Eng R: Reports* 1997;21:101–70.
- [52] Budgett HM. The adherence of flat surfaces. *Proc R Soc London A* 1911;86:25–35.
- [53] Melrose JC. Chemical potential changes in capillary condensation. *J Colloid Interface Sci* 1972;38:312–22.
- [54] Iwamatsu M, Horii K. Capillary condensation and adhesion of two wetter surfaces. *J Colloid Interface Sci* 1996;182:400–6.
- [55] Mate CM, Novotny VJ. Molecular conformation and disjoining pressure of polymeric liquid films. *J Chem Phys* 1991;94:8420–7.
- [56] Preuss M, Butt H-J. Direct measurement of forces between particles and bubbles. *Int J Miner Process* 1999;56:99–115.
- [57] Butt H-J, Kappl M. Normal capillary forces. *Adv Colloid Interface Sci* 2009;146:48–60.
- [58] Anachkov SE, Lesov I, Zanini M, Kralchevsky PA, Denkov ND, Isa L. Particle detachment from fluid interfaces: theory vs. experiments. *Soft Matter* 2016;12:7632–43.
- [59] Delaunay C. Sur la surface de révolution dont la courbure moyenne est constante. *J Math Pures Appl* 1841;6:309–20. [http://portail.mathdoc.fr/JMPA/afficher\\_notice.php?id=JMPA\\_1841\\_1\\_6\\_A24\\_0](http://portail.mathdoc.fr/JMPA/afficher_notice.php?id=JMPA_1841_1_6_A24_0).
- [60] Plateau J. Experimental and theoretical researches on the figures of equilibrium of a liquid mass withdrawn from the action of gravity. *Philos Mag* 1857;14:1–22.
- [61] Rayleigh LXVI. On the instability of a cylinder of viscous liquid under capillary force. *Philos Mag* 1892;34:145–54.
- [62] Mason G, Clark WC. Liquid bridges between spheres. *Chem Eng Sci* 1965;20:859–66.
- [63] Clark WC, Haynes JM, Mason G. Liquid bridges between a sphere and a plane. *Chem Eng Sci* 1968;23:810–2.
- [64] Erle MA, Dyson DC, Morrow NR. Liquid bridges between cylinders, in a torus, and between spheres. *AIChE J* 1971;17:115–21.
- [65] Petkov PV, Radoev BP. Statics and dynamics of capillary bridges. *Colloids Surf A* 2014;460:18–27.
- [66] Melrose JC. Model calculations for capillary condensation. *AIChE J* 1966;12:986–94.
- [67] Princen HM. In: Matijevic E, editor. Surface and colloid science. New York: Wiley-Interscience; 1969. p. 1–84.
- [68] Kralchevsky PA, Nagayama K. Particles at Fluid Interfaces and Membranes. Amsterdam: Elsevier; 2001(Chapters 2 and 11).
- [69] Willett CD, Adams MJ, Johnson SA, Seville JPK. Capillary bridges between two spherical bodies. *Langmuir* 2000;16:9396–405.
- [70] Michael DH. Meniscus stability. *Ann Rev Fluid Mech* 1981;13:189–219.
- [71] Myshkis AD, Babskii VG, Kopachevskii ND, Slobozhanin LA, Tuptsov AD. Low-Gravity Fluid Mechanics: Mathematical Theory of Capillary Phenomena. Springer-Verlag; 1987.
- [72] Lowry BJ, Steen PH. Capillary surfaces: stability from families of equilibria with application to the liquid bridge. *Proc R Soc London A* 1995;449:411–39.
- [73] Vogel TI. Stability of a liquid drop trapped between two parallel planes II: general contact angles. *SIAM J Appl Math* 1989;49:1009–28.
- [74] Vogel TI. Comments on radially symmetric liquid bridges with inflected profiles. *Dynam Contin Discret Impuls Syst (Supplement)* 2005:862–7.
- [75] Vogel TI. Convex, rotationally symmetric liquid bridges between spheres. *Pacific J Math* 2006;2:367–77.
- [76] Vogel TI. Liquid bridges between balls: the small volume instability. *J Math Fluid Mech* 2013;15:397–413.
- [77] Vogel TI. Liquid bridges between contacting balls. *J Math Fluid Mech* 2014;16:737–44.
- [78] Radoev B, Ivanov IT, Petkov P. Capillary bridge: transition from equilibrium to hydrodynamic state. *Colloids Surf A* 2016;505:98–105.
- [79] Petkov PV, Danov KD, Kralchevsky PA. Surface pressure isotherm for a monolayer of charged colloidal particles at a water/nonpolar-fluid interface: experiment and theoretical model. *Langmuir* 2014;30:2768–78.
- [80] Aveyard R, Clint JH, Nees D, Paunov VN. Compression and structure of monolayers of charged latex particles at air/water and octane/water interfaces. *Langmuir* 2000;16:1969–79.
- [81] Danov KD, Kralchevsky PA, Boneva MP. Electrodipping force acting on solid particles at a fluid interface. *Langmuir* 2004;20:6139–51.
- [82] Botto L, Preuss K, Robertson LX, Physical Xu XY. Characterisation and yield stress of a concentrated *Miscanthus* suspension. *Rheologica Acta* 2014;53:805–15.
- [83] Kralchevsky PA, Denkov ND, Danov KD. Particles with an undulated contact line at a fluid interface: interaction between capillary quadrupoles and rheology of particulate monolayers. *Langmuir* 2001;17:7694–705.
- [84] Buttinoni I, Zell ZA, Squires TM, Isa L. Colloidal binary mixtures at fluid–fluid interfaces under steady shear: structural, dynamical and mechanical response. *Soft Matter* 2015;11:8313–21.
- [85] Buttinoni I, Steinacher M, Spanke HT, Pokki J, Bahmann S, Nelson B, et al. Colloidal polycrystalline monolayers under oscillatory shear. *Phys Rev E* 2017;95:012610.
- [86] Vankova N, Tcholakova S, Denkov ND, Ivanov IB, Vulchev VD, Danner T. Emulsification in turbulent flow: 1. Mean and maximum drop diameters in inertial and viscous regimes. *J Colloid Interface Sci* 2007;312:363–80.
- [87] Krieger LM, Dougherty TJA. Mechanism for non-Newtonian flow in suspensions of rigid spheres. *Journal of Rheology* 1959;3:137–52.
- [88] Russel WB, Saville DA, Schowalter WR. Colloidal Dispersions. Cambridge University Press; 1989.
- [89] Yamaki M, Higo J, Nagayama K. Size-dependent separation of colloidal particles in two-dimensional convective self-assembly. *Langmuir* 1995;11:2975–8.
- [90] Starov VM. Equilibrium and hysteresis contact angles. *Adv Colloid Interface Sci* 1982;39:147–73.
- [91] Marmur A. Thermodynamic aspects of contact angle hysteresis. *Adv Colloid Interface Sci* 1994;50:121–41.
- [92] Iliev SD. Static drops on an inclined plane: equilibrium modeling and numerical analysis. *J Colloid Interface Sci* 1997;194:287–300.
- [93] Brutin D, Starov V. Recent advances in droplet wetting and evaporation. *Chem Soc Rev* 2018. <https://doi.org/10.1039/C6CS00902F>.

# Supplementary material

for the article

## Hardening of particle/oil/water suspensions due to capillary bridges: Experimental yield stress and theoretical interpretation

Krassimir D. Danov<sup>a</sup>, Mihail T. Georgiev<sup>a</sup>, Peter A. Kralchevsky<sup>a,\*</sup>, Gergana M. Radulova<sup>a</sup>,  
Theodor D. Gurkov<sup>a</sup>, Simeon D. Stoyanov<sup>b,c,d</sup>, Eddie G. Pelan<sup>b</sup>

<sup>a</sup> *Department of Chemical & Pharmaceutical Engineering, Faculty of Chemistry and  
Pharmacy, Sofia University, Sofia 1164, Bulgaria*

<sup>b</sup> *Unilever Research & Development Vlaardingen, 3133AT Vlaardingen, The Netherlands*

<sup>c</sup> *Laboratory of Physical Chemistry and Colloid Science, Wageningen University, 6703 HB  
Wageningen, The Netherlands*

<sup>d</sup> *Department of Mechanical Engineering, University College London, WC1E 7JE, UK*

### Appendix A. System of equations and computational procedure

#### 1. Basic equations

For the computations, it is convenient to scale all quantities with dimension of length using the particle radius,  $a$ ; the dimensionless quantities will be denoted by tilde:

$$\tilde{r} = \frac{r}{a}, \quad \tilde{z} = \frac{z}{a}, \quad \tilde{r}_c = \frac{r}{a}, \quad \tilde{z}_c = \frac{r}{a}, \quad \tilde{r}_0 = \frac{r_0}{a}, \quad \tilde{h} = \frac{h}{2a} \quad (\text{A.1})$$

For the meaning of the geometrical parameters, see Fig. 11a in the main text.

Here, our goal is to compute (i) the profile of the capillary bridges; (ii) the dimensionless capillary force,  $f = f(\tilde{h}, \Phi, \alpha)$ ; (iii) the dimensionless shear-response force,  $f_{\text{sh}} = f_{\text{sh}}(\gamma, \Phi, \alpha)$ , and the maximum value of  $f_{\text{sh}}$  with respect to  $\gamma$ :  $f_{\text{max}} = f_{\text{sh,max}}(\Phi, \alpha)$ . As in the main text,  $h$  is the surface-to-surface distance between the two spherical particles connected by the capillary bridge;  $\Phi = V_i/V_p$  is the dimensionless bridge volume, see Fig. 11a in the main text;  $\alpha$  is the three-phase contact angle measured across the bridge phase, and  $\gamma$  is the shearing angle (Fig. 10b).

In view of Eq. (A.1), the dimensionless form of Eqs. (8)–(12) in the main text is:

$$x = \left| \tilde{r} / \tilde{r}_0 - 1 \right|^{1/2} \quad (\text{A.2})$$

$$\tilde{z}(x) = 2\tilde{r}_0 \int_0^x \frac{1 + p\xi^2(2 + \xi^2)}{[(2 + \xi^2)(1 - 2p - 2p^2\xi^2 - p^2\xi^4)]^{1/2}} d\xi \quad (p < 0.5) \quad (\text{A.3a})$$

$$\tilde{z}(x) = 2\tilde{r}_0 \int_0^x \frac{1 - p\xi^2(2 - \xi^2)}{[(2 - \xi^2)(2p - 1 - 2p^2\xi^2 + p^2\xi^4)]^{1/2}} d\xi \quad (p > 0.5) \quad (\text{A.3b})$$

$$p = \frac{\tilde{r}_0^2 - \tilde{r}_0\tilde{r}_c \sin \theta_c}{\tilde{r}_0^2 - \tilde{r}_c^2} \quad (\text{A.4})$$

$$f = (1 - p)\tilde{r}_0 \quad (\text{A.5})$$

At the contact line on the particle surface,  $(r, z) = (r_c, z_c)$ , Eqs. (A.2)–(A.3) acquire the form:

$$x_c = |\tilde{r}_c / \tilde{r}_0 - 1|^{1/2} \quad (\text{A.6})$$

$$\tilde{z}_c = 2\tilde{r}_0 \int_0^{x_c} \frac{1 + p\xi^2(2 + \xi^2)}{[(2 + \xi^2)(1 - 2p - 2p^2\xi^2 - p^2\xi^4)]^{1/2}} d\xi \quad (p < 0.5) \quad (\text{A.7a})$$

$$\tilde{z}_c = 2\tilde{r}_0 \int_0^{x_c} \frac{1 - p\xi^2(2 - \xi^2)}{[(2 - \xi^2)(2p - 1 - 2p^2\xi^2 + p^2\xi^4)]^{1/2}} d\xi \quad (p > 0.5) \quad (\text{A.7b})$$

The volume confined between the surface of the capillary bridge and the two horizontal planes  $z = 0$  and  $z = z_c$  (see Fig. 11a), is:

$$V_c = \pi \int_0^{z_c} r^2 dz = \pi \int_{r_0}^{r_c} r^2 \frac{dz}{dr} dr \quad (\text{A.8})$$

Likewise, the area of the capillary meniscus of the bridge is:

$$A_c = 2\pi \int_0^{z_c} \frac{r}{\sin \theta} dz = 2\pi \int_{r_0}^{r_c} \frac{r}{\sin \theta} \frac{dz}{dr} dr \quad (\text{A.9})$$

Next, we introduce dimensionless variables in accordance with Eq. (A.1), express the derivative  $d\tilde{z}/dx$  from Eq. (A.3) and  $\sin \theta$  from Eq. (4) in the main text. Thus, we obtain:

$$\tilde{V}_c \equiv \frac{V_c}{a^3} = 2\pi\tilde{r}_0^3 \int_0^{x_c} \frac{[1 + px^2(2 + x^2)](1 + x^2)^2}{[(2 + x^2)(1 - 2p - 2p^2x^2 - p^2x^4)]^{1/2}} dx \quad (p < 0.5) \quad (\text{A.10a})$$

$$\tilde{V}_c \equiv \frac{V_c}{a^3} = 2\pi\tilde{r}_0^3 \int_0^{x_c} \frac{[1 - px^2(2 - x^2)](1 - x^2)^2}{[(2 - x^2)(2p - 1 - 2p^2x^2 + p^2x^4)]^{1/2}} dx \quad (p > 0.5) \quad (\text{A.10b})$$

$$\tilde{A}_c = \frac{A_c}{a^2} = 4\pi\tilde{r}_0^2 \int_0^{x_c} \frac{(1+x^2)^2}{[(2+x^2)(1-2p-2p^2x^2-p^2x^4)]^{1/2}} dx \quad (p < 0.5) \quad (\text{A.11a})$$

$$\tilde{A}_c = \frac{A_c}{a^2} = 4\pi\tilde{r}_0^2 \int_0^{x_c} \frac{(1-x^2)^2}{[(2-x^2)(2p-1-2p^2x^2+p^2x^4)]^{1/2}} dx \quad (p > 0.5) \quad (\text{A.11b})$$

From Fig. 11a, we find the following relations between the geometrical parameters:

$$r_c = a \sin \varphi_c, \quad z_c = \frac{h}{2} + a - a \cos \varphi_c, \quad \theta_c = \alpha + \varphi_c \quad (\text{A.12})$$

In view of Eq. (A.1), the dimensionless form of Eq. (A.12) is:

$$\tilde{r}_c = \sin \varphi_c, \quad \tilde{z}_c = \tilde{h} + 1 - \cos \varphi_c, \quad \theta_c = \alpha + \varphi_c \quad (\text{A.13})$$

The volume of the liquid in the upper part of the capillary bridge,  $V_i$ , is equal to the difference between  $V_c$  and the respective part of the particle volume (Fig. 11a):

$$V_i = V_c - \frac{\pi}{3} \left(z_c - \frac{h}{2}\right)^2 \left(3a + \frac{h}{2} - z_c\right) \quad (\text{A.14})$$

Then, the dimensionless bridge volume,  $\Phi$ , can be expressed in the form:

$$\Phi \equiv \frac{V_i}{V_p} = \frac{3V_i}{4\pi a^3} = \frac{3\tilde{V}_c}{4\pi} - \frac{1}{4} (\tilde{z}_c - \tilde{h})^2 (3 + \tilde{h} - \tilde{z}_c) \quad (\text{A.15})$$

What concerns the shear deformation we will assume that in the initial state the surfaces of the two particles touch each other (Fig. 10). Then, Eq. (20) in the main text with  $L = 2a$  and  $\varepsilon = \tan \gamma$  acquires the form:

$$h = 2a(1 + \tan^2 \gamma)^{1/2} - 2a \quad (\text{A.16})$$

From Eq. (A.16) we obtain an expression for determining  $\gamma$ :

$$\tan \gamma = [(\tilde{h} + 1)^2 - 1]^{1/2} \quad (\text{A.17})$$

Finally, in accordance with Eq. (17) and (A.5)

$$f_{\text{sh}} \equiv f \sin \gamma = (1-p)\tilde{r}_0 \sin \gamma \quad (\text{A.18})$$

## 2. Computational procedure for the bridge profile

In this case, our goal is to compute the function  $\tilde{z} = \tilde{z}(\tilde{r})$  for a capillary bridge that connects two spherical particles of radius  $a$ , separated at a surface-to-surface distance  $h$ . The input parameters are  $\tilde{r}_c, \tilde{h}$  and  $\alpha$ . The steps of the computational procedure are as follows:

- 1) From Eq. (A.13), we calculate  $\varphi_c, \tilde{z}_c$  and  $\theta_c$ .
- 2) We give a tentative value to  $\tilde{r}_0$  to start a procedure for determining  $\tilde{r}_0$  by the bisection method.
- 3) From Eqs. (A.4) and (A.6), we determine  $p$  and  $x_c$ .
- 4) With the value of  $\tilde{z}_c$  from point 1, we determine  $\tilde{r}_0$  by solving Eq. (A.7) numerically using the bisection method. The integral in Eq. (A.7) is calculated numerically using the Simpson method.
- 5) With the determined value of  $\tilde{r}_0$ , the meniscus profile  $\tilde{z} = \tilde{z}(\tilde{r})$  is computed from Eq. (A.3), using the Simpson method to calculate the integral numerically.

## 3. Computational procedure for $f(\tilde{h}, \Phi, \alpha)$ , $f_{\text{sh}}(\gamma, \Phi, \alpha)$ and $f_{\text{max}}(\Phi, \alpha)$

The input parameters are  $\tilde{h}, \Phi$  and  $\alpha$ . The steps of the computational procedure are as follows:

- 1) We give a tentative value to  $\tilde{r}_c$  to start a procedure for determining  $\tilde{r}_c$  by the bisection method.
- 2) From Eq. (A.13), we calculate  $\varphi_c, \tilde{z}_c$  and  $\theta_c$ .
- 3) We give a tentative value to  $\tilde{r}_0$  to start a procedure for determining  $\tilde{r}_0$  by the bisection method.
- 4) From Eqs. (A.4) and (A.6), we determine  $p$  and  $x_c$ .
- 5) With the value of  $\tilde{z}_c$  from point 1, we determine  $\tilde{r}_0$  by solving Eq. (A.7) numerically using the bisection method. The integral in Eq. (A.7) is calculated numerically using the Simpson method.
- 6) With the determined value of  $\tilde{r}_0$ , we calculate  $\tilde{V}_c$  from Eq. (A.10).
- 7) For each given  $\Phi$ , we determine  $\tilde{r}_c$  by solving Eq. (A.15) numerically using the bisection method.
- 8) The dimensionless capillary force  $f$  is calculated from Eq. (A.5).

9) The shearing angle  $\gamma$  and the dimensionless shear-response force  $f_{sh}$  are calculated from Eqs. (A.17) and (A.18).

10)  $f_{max}$  is determined as the maximal value of  $f_{sh}$ .

## Appendix B. Additional experimental and computational results

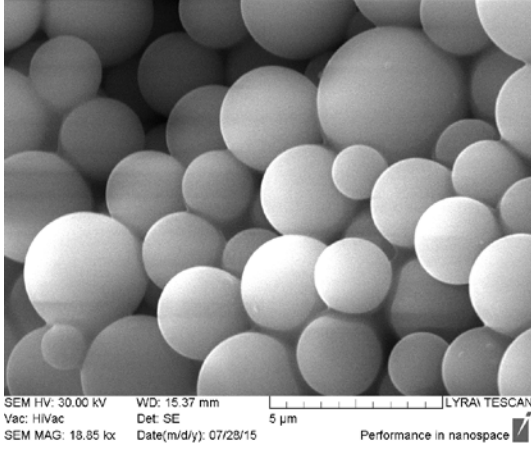


**Fig. S1.** SEM image of the used silica particles.

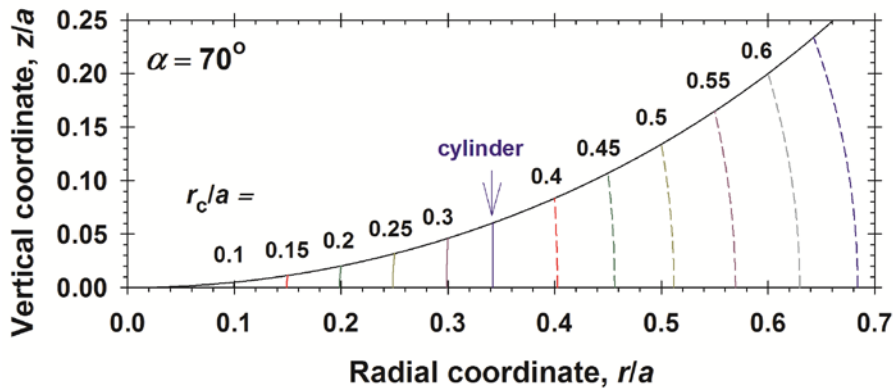


**Fig. S2.** Calculated profiles of capillary bridges,  $z(r)$ , for increasing bridge volume; the contact angle is fixed,  $\alpha = 70^\circ$ , whereas the position of the contact line, characterized by its radius,  $r_c$ , varies;  $r$  and  $z$  are cylindrical coordinates; the bridge connects two identical spherical particles of radius  $a$ , which are in a contact,  $h = 0$ . All profiles do not possess inflection points. For all of them, the capillary-bridge force,  $F_{cap}$ , is attractive. The rightmost profile corresponds to sphere with  $F_{cap} = 0$ .

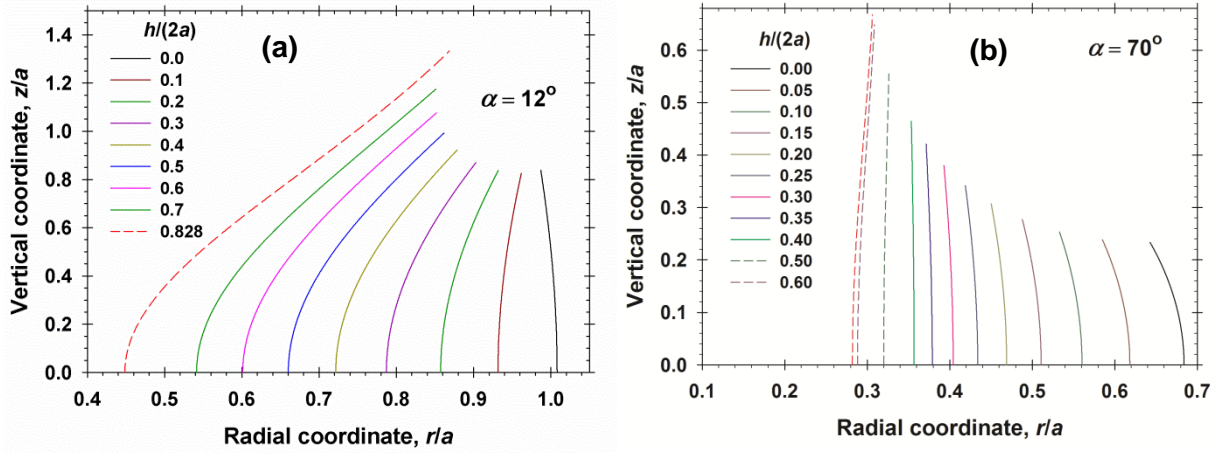


**Fig. S3.** Calculated profiles of a capillary bridge of fixed volume at different degrees of extension, i.e., at different distances,  $h$ , between the surfaces of two identical particles of radius  $a$ . (a)  $\alpha = 12^\circ$  and  $\Phi = 0.25$ . (b)  $\alpha = 70^\circ$  and  $\Phi = 0.041$ ; the dashed profiles possess inflection point and could be unstable [73,74]. The leftmost red curves correspond to the greatest possible  $h$ ; for greater  $h$  the Laplace equation has no solution.

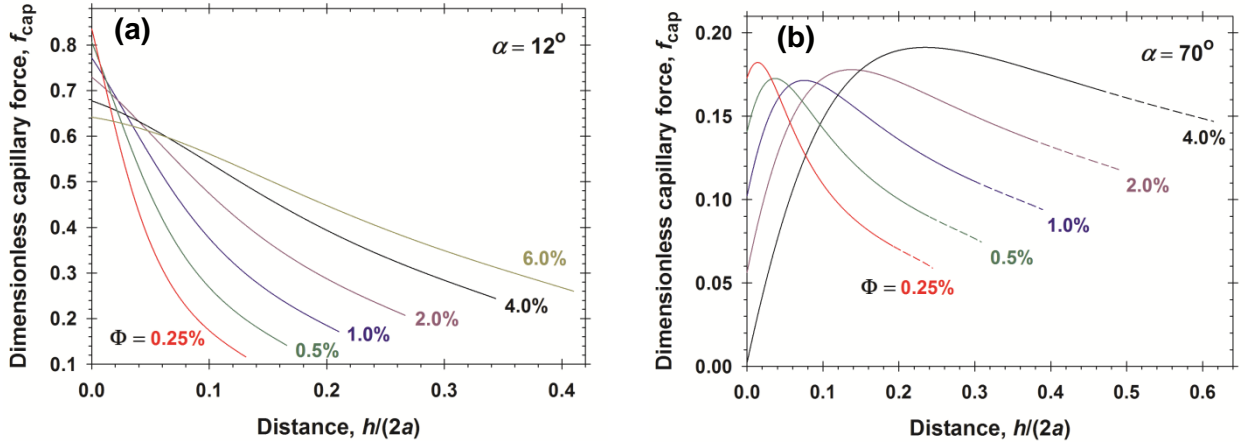


**Fig. S4.** Calculated dependences of the *dimensionless capillary force*,  $f_{\text{cap}} = F_{\text{cap}}/(2\pi a\sigma)$ , on the dimensionless surface-to-surface distance between the particles  $\tilde{h} = h/(2a)$ , at different values of the dimensionless bridge volume,  $\Phi$ , and for contact angles: (a)  $\alpha = 12^\circ$ . (b)  $\alpha = 70^\circ$ ; the dashed portions of the lines correspond to unduloids with inflection point, which could correspond to unstable bridges [73,74].

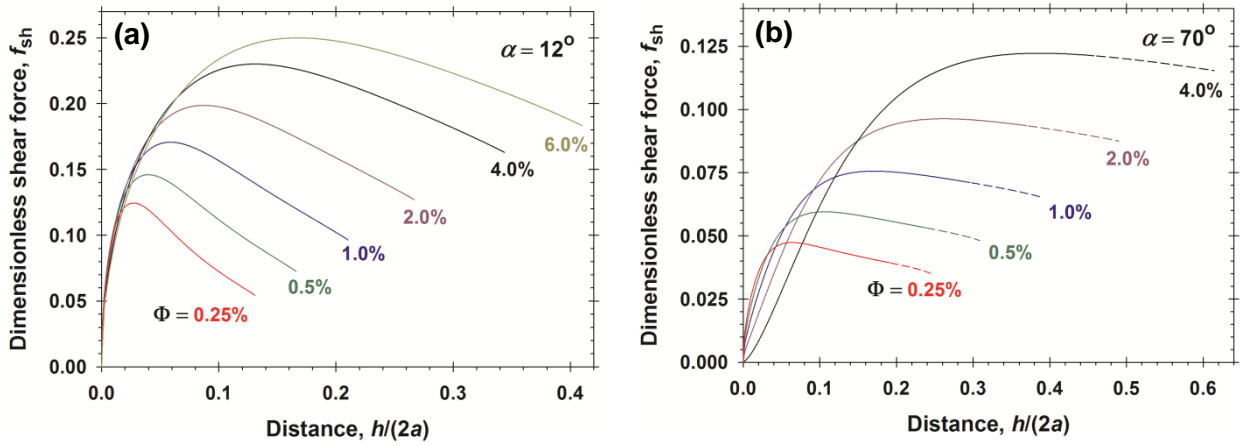


**Fig. S5.** Calculated dependences of the *dimensionless force of shear response*,  $f_{sh} = f_{cap} \sin \gamma$ , on dimensionless surface-to-surface distance between the particles  $\tilde{h} = h(2a)$  at different values of the dimensionless bridge volume,  $\Phi$ , and for contact angles: (a)  $\alpha = 12^\circ$ . (b)  $\alpha = 70^\circ$ ; the dashed portions of the lines correspond to unduloids with inflection point, which could correspond to unstable bridges [73,74].

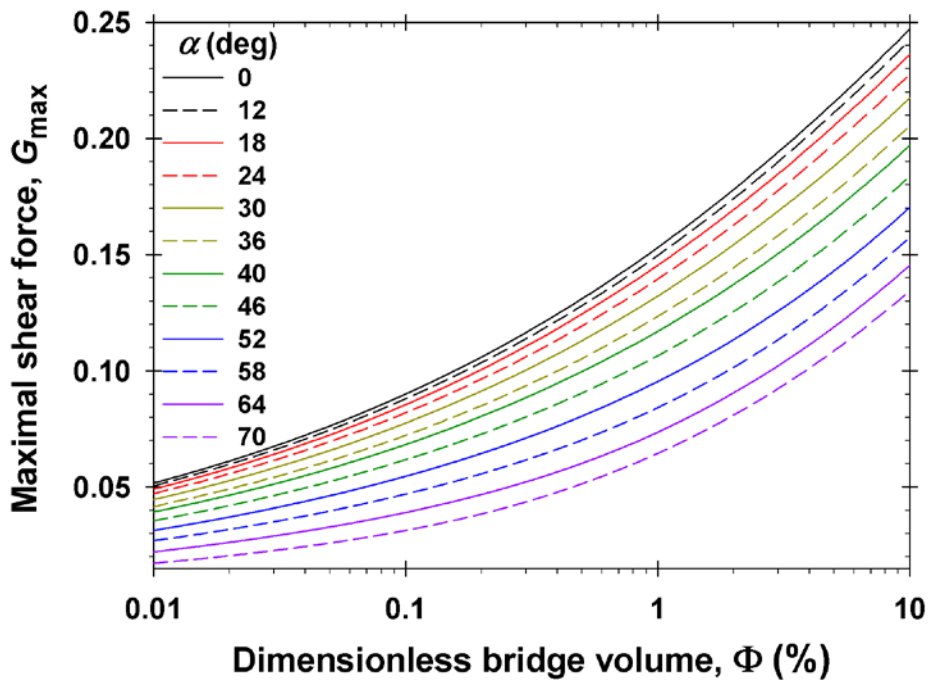


**Fig. S6.** Plane-parallel deformation zone: Calculated plot of the maximal dimensionless shear force,  $G_{max}$ , vs. the dimensionless bridge volume,  $\Phi$ , for various values of the contact angle,  $\alpha$ .



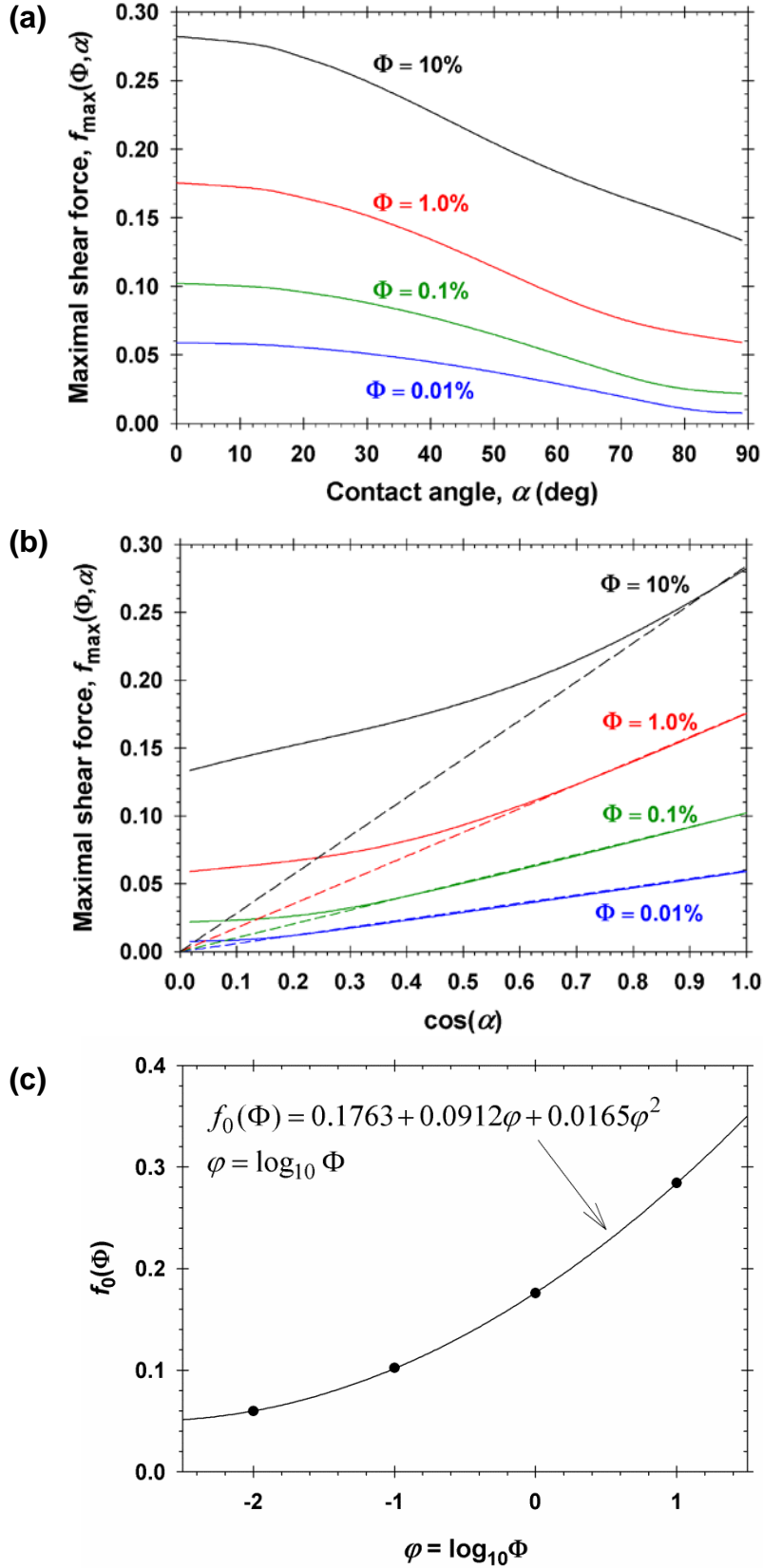


**Fig. S7.** Plots of the computed maximal value of the dimensionless force of shear response,  $f_{\max}$ , (a) versus the contact angle  $\alpha$  and (b) versus  $\cos\alpha$ , for various values of the dimensionless bridge volume  $\Phi$ ; the dashed straight lines are drawn according to the equation  $f_{\max}(\Phi, \alpha) = f_0(\Phi)\cos\alpha$ ; see Table B1. (c) Interpolation of the data for  $f_0(\Phi)$  in Table B1.

**Table B1.** Data for the dashed straight lines in Fig. S7b:  $f_{\max}(\Phi, \alpha) \approx f_0(\Phi) \cos \alpha$  for  $\alpha \leq \alpha_0$ .

$\Phi$ (%)	$f_0(\Phi)$	$\alpha_0$ (deg)	$\cos \alpha_0$ (deg)
0.01	0.05968	80.5	0.165
0.1	0.1021	68.5	0.367
1	0.1758	51.5	0.623
10	0.2842	29.5	0.870

An accurate interpolation of the data for  $f_0(\Phi)$  in Table B1 yields (see Fig. S7c):

$$f_{\max}(\Phi, \alpha) \approx (0.1763 + 0.0912\varphi + 0.0165\varphi^2) \cos \alpha \text{ for } \alpha \leq \alpha_0 \quad (\text{B.1})$$

$$\alpha_0(\text{deg}) = 51.5 - 19.5\varphi - 2.5\varphi^2, \quad \varphi = \log_{10} \Phi(\%)$$

where  $0.01\% \leq \Phi \leq 10\%$ . Eq. (B.1) is appropriate for fast estimates. The tabulated exact function  $f_{\max}(\Phi, \alpha)$  is given in Table C1 (Appendix C).

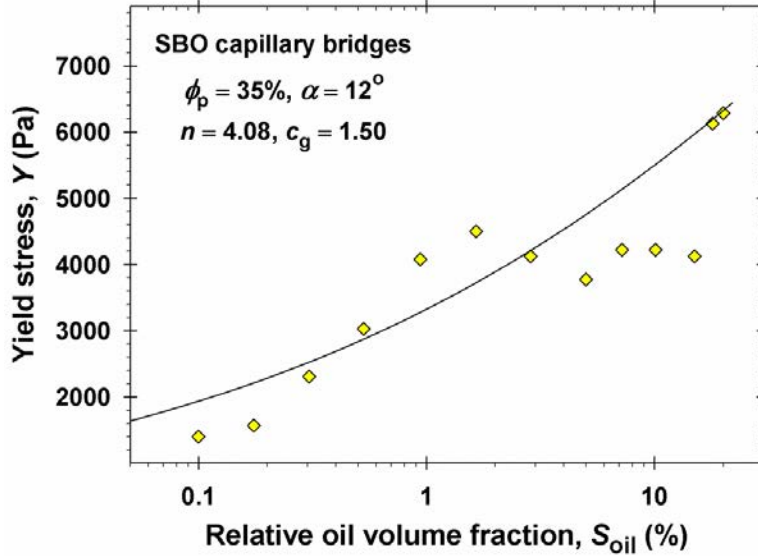


**Fig. S8.** Suspension with capillary bridges from soybean oil (SBO) in water: Plot of the measured yield stress,  $Y$ , vs. the relative oil volume fraction,  $S_{\text{oil}}$ , for hydrophobized silica particles of contact angle  $\alpha = 12^\circ$  across the SBO at particle volume fraction  $\phi_p = 35\%$ ; the mean number of capillary bridges per particle,  $n$ , is calculated from Eq. (2) in the main text. The solid line is the theoretical curve calculated with geometrical coefficient  $c_g = 1.5$ .

For the system corresponding to Fig. S8 (capillary bridges from SBO in water,  $\phi_p = 35\%$ ), we have only a single set of data, because the particles from the used batch were over, but the particles from the new batch showed a systematic deviation (lower  $Y$ ) probably due to a different contact angle. Despite the greater scattering of the points in Fig. S8 (as compared to Fig. 8 in the main text), the theoretical curve is in agreement with the overall tendency of the experimental data in Fig. S8.

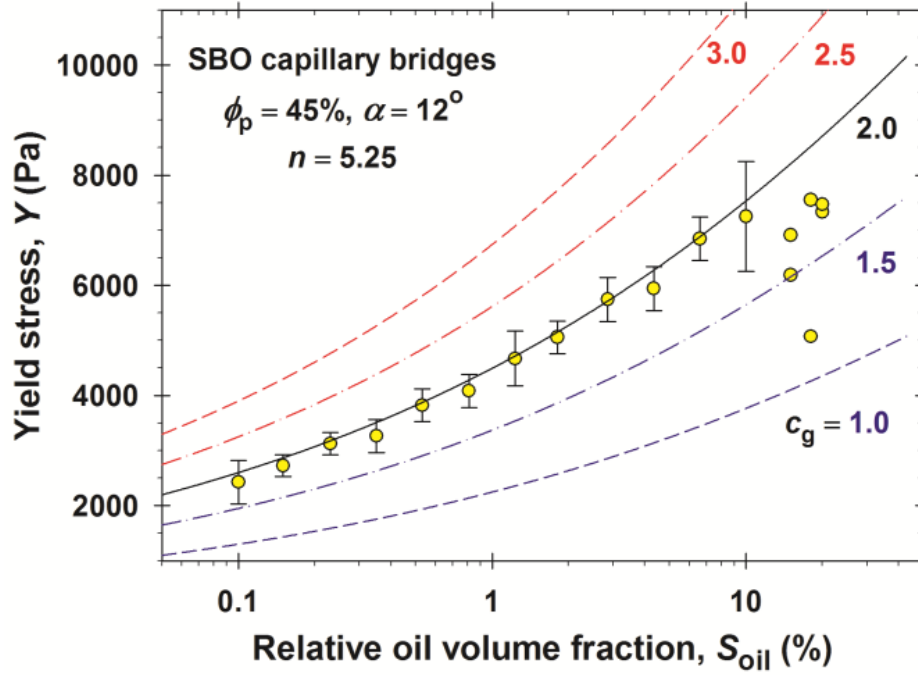


**Fig. S9.** Illustration of the effect of geometrical parameter  $c_g$  on the calculated theoretical curves: Plots of the yield stress,  $Y$ , vs.  $S_{oil}$  for SBO capillary bridges at  $\alpha = 12^\circ$  and  $\phi_p = 45\%$ . The best fit corresponds to  $c_g \approx 2$ .

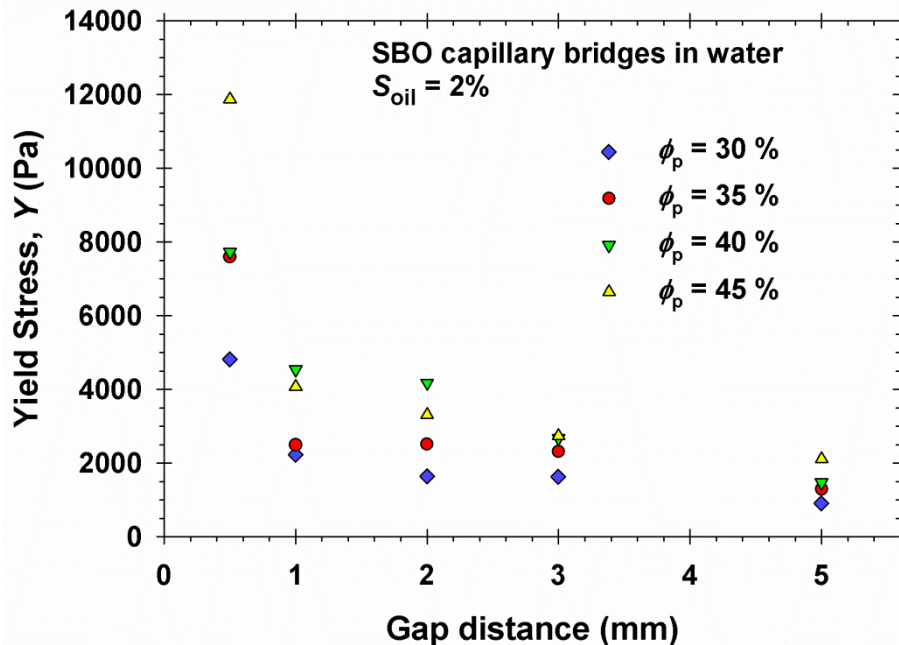


**Fig. S10.** Plot of experimental data for the yield stress  $Y$  vs. the width of the gap between the two parallel disks of the rheometer for various particle volume fractions,  $\phi_p$ , at fixed relative volume fraction of SBO,  $S_{oil} = 2\%$ .

As an illustration, Fig. S9 (capillary bridges from SBO in water,  $\phi_p = 45\%$ ) shows theoretical curves calculated for five different values of the geometrical coefficient  $c_g$  in Eq. (32). The curve with  $c_g = 2$  provides the best fit.

The model of the deformation zone in its two versions (plane-parallel and conical deformation zone) predicts that the *yield stress*  $Y$  has to be independent of the geometry of the deformation zone, whereas the *yield strain*  $\psi_Y$  depends on the geometry of the deformation zone characterized by the parameter  $d$  or  $\beta$  (see Figs. 14a and 14c in the main article and the related text). This theoretical prediction means that  $Y$  has to be independent of the gap distance (the distance between the two parallel disks of the rotational rheometer). This prediction is verified in Fig. S10.

The data in Fig. S10 indicate that  $Y$  really exhibits a tendency to level off to a constant value for gap distance greater than 1–2 mm. At shorter gap distances,  $Y$  strongly increases. In terms of the conical model (Fig. 14c) this could be interpreted as a contact of the zone of deformation (of its outer part) with the lower (fixed) disk, where local wall-slip could take place. The implication from this experiment (provoked by the comparison of theory and experiment) is that before carrying out systematic measurements, one should check the dependence of the yield stress  $Y$  on the gap distance and to work with gap distances from the plateau region (Fig. S10). In our systematic measurements, the gap distance was set 2 mm, which is in the beginning of the plateau region. Hence, we could expect that our data for the yield stress,  $Y$ , are not essentially influenced by the geometry of the experimental cell.

### **Appendix C. Database and interpolation formula for calculating the yield stress**

To calculate the yield stress from Eq. (33) in the main text, one needs the values of the universal function  $f_{\max}(\Phi, \alpha)$ . This function has been calculated numerically using the exact theory of the capillary bridges, as explained in Appendix A, and tabulated in Table C1 (see the next page). The data in Table C1 (available also as an attached Excel file) can be used as a database for calculating  $f_{\max}(\Phi, \alpha)$  for given values of  $\Phi$  and  $\alpha$ . Because  $\Phi$  varies by orders of magnitude, it is convenient to work with the quantity  $\varphi = \log_{10}\Phi$ .

If  $\varphi$  belongs to the interval  $\varphi_1 \leq \varphi \leq \varphi_2$  and  $\alpha$  belongs to the interval  $\alpha_1 \leq \alpha \leq \alpha_2$ , where  $\varphi_1$ ,  $\varphi_2$ ,  $\alpha_1$  and  $\alpha_2$  are values given in Table C1, then  $f_{\max}(\varphi, \alpha)$  can be calculated from the following four-point interpolation formula:

$$\begin{aligned}
 f(\varphi, \alpha) = & \frac{(\varphi - \varphi_2)(\alpha - \alpha_2)}{(\varphi_1 - \varphi_2)(\alpha_1 - \alpha_2)} f(\varphi_1, \alpha_1) + \frac{(\varphi - \varphi_2)(\alpha - \alpha_1)}{(\varphi_1 - \varphi_2)(\alpha_2 - \alpha_1)} f(\varphi_1, \alpha_2) \\
 & + \frac{(\varphi - \varphi_1)(\alpha - \alpha_2)}{(\varphi_2 - \varphi_1)(\alpha_1 - \alpha_2)} f(\varphi_2, \alpha_1) + \frac{(\varphi - \varphi_1)(\alpha - \alpha_1)}{(\varphi_2 - \varphi_1)(\alpha_2 - \alpha_1)} f(\varphi_2, \alpha_2)
 \end{aligned} \tag{D.1}$$

Eq. (D.1) can be programmed in the computer and Table C1 (see the next page and the appended Excel file) can be used as a database for calculating  $f_{\max}(\varphi, \alpha)$ , where  $\varphi = \log_{10} \Phi$ .

(see Table C1 on the next page)

**Table C1.** Database representing the dependence of  $f_{\max}$  on the volume fraction  $\Phi$  and three phase contact angle  $\alpha$ .

$-\log_{10}\Phi$	Three phase contact angle, $\alpha$ (deg)											
	0	12	18	24	30	36	40	46	52	58	64	70
4.00	0.0590	0.0577	0.0561	0.0538	0.0509	0.0475	0.0449	0.0406	0.0358	0.0307	0.0253	0.0197
3.97	0.0600	0.0587	0.0570	0.0547	0.0518	0.0483	0.0456	0.0413	0.0364	0.0312	0.0257	0.0200
3.94	0.0610	0.0597	0.0580	0.0556	0.0526	0.0491	0.0464	0.0420	0.0370	0.0318	0.0261	0.0203
3.91	0.0621	0.0607	0.0590	0.0566	0.0535	0.0499	0.0472	0.0427	0.0377	0.0323	0.0266	0.0207
3.88	0.0631	0.0617	0.0599	0.0575	0.0544	0.0507	0.0480	0.0434	0.0383	0.0328	0.0270	0.0210
3.85	0.0642	0.0628	0.0610	0.0585	0.0554	0.0516	0.0488	0.0441	0.0389	0.0334	0.0275	0.0214
3.82	0.0653	0.0638	0.0620	0.0595	0.0563	0.0525	0.0496	0.0448	0.0396	0.0339	0.0280	0.0218
3.79	0.0664	0.0649	0.0630	0.0605	0.0572	0.0534	0.0504	0.0456	0.0403	0.0345	0.0284	0.0222
3.76	0.0675	0.0660	0.0641	0.0615	0.0582	0.0543	0.0513	0.0464	0.0409	0.0351	0.0289	0.0225
3.73	0.0687	0.0671	0.0652	0.0625	0.0592	0.0552	0.0521	0.0471	0.0416	0.0357	0.0294	0.0229
3.70	0.0698	0.0682	0.0663	0.0636	0.0602	0.0561	0.0530	0.0479	0.0423	0.0363	0.0299	0.0233
3.67	0.0710	0.0694	0.0674	0.0647	0.0612	0.0570	0.0539	0.0487	0.0430	0.0369	0.0304	0.0238
3.64	0.0722	0.0706	0.0685	0.0657	0.0622	0.0580	0.0548	0.0496	0.0438	0.0375	0.0309	0.0242
3.61	0.0734	0.0717	0.0697	0.0668	0.0633	0.0590	0.0557	0.0504	0.0445	0.0381	0.0315	0.0246
3.58	0.0746	0.0729	0.0709	0.0680	0.0643	0.0599	0.0567	0.0512	0.0452	0.0388	0.0320	0.0250
3.55	0.0759	0.0742	0.0720	0.0691	0.0654	0.0610	0.0576	0.0521	0.0460	0.0394	0.0325	0.0255

$-\log_{10}\Phi$	Three phase contact angle, $\alpha$ (deg)											
	0	12	18	24	30	36	40	46	52	58	64	70
3.52	0.0772	0.0754	0.0733	0.0703	0.0665	0.0620	0.0586	0.0530	0.0468	0.0401	0.0331	0.0260
3.49	0.0785	0.0767	0.0745	0.0714	0.0676	0.0630	0.0596	0.0538	0.0475	0.0408	0.0337	0.0264
3.46	0.0798	0.0780	0.0757	0.0726	0.0687	0.0641	0.0605	0.0547	0.0483	0.0415	0.0342	0.0269
3.43	0.0811	0.0793	0.0770	0.0739	0.0699	0.0651	0.0616	0.0556	0.0491	0.0422	0.0348	0.0274
3.40	0.0825	0.0806	0.0783	0.0751	0.0710	0.0662	0.0626	0.0566	0.0500	0.0429	0.0354	0.0279
3.37	0.0838	0.0819	0.0796	0.0763	0.0722	0.0673	0.0636	0.0575	0.0508	0.0436	0.0360	0.0284
3.34	0.0852	0.0833	0.0809	0.0776	0.0734	0.0684	0.0647	0.0585	0.0516	0.0443	0.0366	0.0289
3.31	0.0867	0.0847	0.0823	0.0789	0.0747	0.0696	0.0658	0.0594	0.0525	0.0451	0.0373	0.0295
3.28	0.0881	0.0861	0.0836	0.0802	0.0759	0.0707	0.0669	0.0604	0.0534	0.0458	0.0379	0.0300
3.25	0.0896	0.0875	0.0850	0.0816	0.0772	0.0719	0.0680	0.0614	0.0543	0.0466	0.0386	0.0306
3.22	0.0911	0.0890	0.0864	0.0829	0.0784	0.0731	0.0691	0.0625	0.0552	0.0474	0.0393	0.0312
3.19	0.0926	0.0905	0.0879	0.0843	0.0797	0.0743	0.0702	0.0635	0.0561	0.0482	0.0399	0.0317
3.16	0.0941	0.0920	0.0893	0.0857	0.0811	0.0755	0.0714	0.0646	0.0570	0.0490	0.0406	0.0324
3.13	0.0957	0.0935	0.0908	0.0871	0.0824	0.0768	0.0726	0.0656	0.0580	0.0498	0.0413	0.0330
3.10	0.0973	0.0951	0.0923	0.0885	0.0838	0.0781	0.0738	0.0667	0.0590	0.0507	0.0421	0.0336
3.07	0.0989	0.0966	0.0938	0.0900	0.0852	0.0794	0.0750	0.0678	0.0599	0.0515	0.0428	0.0343
3.04	0.1005	0.0982	0.0954	0.0915	0.0866	0.0807	0.0762	0.0689	0.0609	0.0524	0.0436	0.0350
3.01	0.1022	0.0998	0.0970	0.0930	0.0880	0.0820	0.0775	0.0701	0.0620	0.0533	0.0444	0.0356
2.98	0.1039	0.1015	0.0986	0.0945	0.0894	0.0834	0.0788	0.0712	0.0630	0.0542	0.0451	0.0364

$-\log_{10}\Phi$	Three phase contact angle, $\alpha$ (deg)											
	0	12	18	24	30	36	40	46	52	58	64	70
2.95	0.1056	0.1032	0.1002	0.0961	0.0909	0.0847	0.0801	0.0724	0.0640	0.0551	0.0460	0.0371
2.92	0.1073	0.1049	0.1018	0.0977	0.0924	0.0861	0.0814	0.0736	0.0651	0.0561	0.0468	0.0379
2.89	0.1091	0.1066	0.1035	0.0993	0.0939	0.0875	0.0827	0.0748	0.0662	0.0570	0.0476	0.0386
2.86	0.1108	0.1083	0.1052	0.1009	0.0955	0.0890	0.0841	0.0761	0.0673	0.0580	0.0485	0.0394
2.83	0.1127	0.1101	0.1069	0.1026	0.0970	0.0904	0.0855	0.0773	0.0684	0.0590	0.0494	0.0402
2.80	0.1145	0.1119	0.1087	0.1042	0.0986	0.0919	0.0869	0.0786	0.0696	0.0600	0.0503	0.0411
2.77	0.1164	0.1137	0.1105	0.1059	0.1002	0.0934	0.0883	0.0799	0.0707	0.0611	0.0512	0.0420
2.74	0.1183	0.1156	0.1123	0.1077	0.1019	0.0949	0.0898	0.0812	0.0719	0.0621	0.0522	0.0429
2.71	0.1202	0.1175	0.1141	0.1094	0.1035	0.0965	0.0912	0.0826	0.0731	0.0632	0.0531	0.0438
2.68	0.1222	0.1194	0.1159	0.1112	0.1052	0.0981	0.0927	0.0839	0.0744	0.0643	0.0541	0.0447
2.65	0.1241	0.1213	0.1178	0.1130	0.1069	0.0997	0.0942	0.0853	0.0756	0.0654	0.0551	0.0457
2.62	0.1261	0.1233	0.1197	0.1148	0.1087	0.1013	0.0958	0.0867	0.0769	0.0665	0.0562	0.0467
2.59	0.1282	0.1253	0.1217	0.1167	0.1104	0.1029	0.0973	0.0881	0.0782	0.0677	0.0573	0.0478
2.56	0.1303	0.1273	0.1236	0.1186	0.1122	0.1046	0.0989	0.0896	0.0795	0.0689	0.0584	0.0488
2.53	0.1324	0.1294	0.1256	0.1205	0.1140	0.1063	0.1005	0.0911	0.0808	0.0701	0.0595	0.0499
2.50	0.1345	0.1314	0.1277	0.1224	0.1159	0.1080	0.1022	0.0926	0.0822	0.0714	0.0606	0.0511
2.47	0.1366	0.1335	0.1297	0.1244	0.1177	0.1098	0.1038	0.0941	0.0836	0.0726	0.0618	0.0523
2.44	0.1388	0.1357	0.1318	0.1264	0.1196	0.1116	0.1055	0.0957	0.0850	0.0739	0.0630	0.0535
2.41	0.1411	0.1379	0.1339	0.1284	0.1216	0.1134	0.1072	0.0972	0.0864	0.0752	0.0643	0.0547



$-\log_{10}\Phi$	Three phase contact angle, $\alpha$ (deg)											
	0	12	18	24	30	36	40	46	52	58	64	70
2.38	0.1433	0.1401	0.1360	0.1305	0.1235	0.1152	0.1090	0.0988	0.0879	0.0766	0.0656	0.0560
2.35	0.1456	0.1423	0.1382	0.1326	0.1255	0.1170	0.1108	0.1005	0.0894	0.0780	0.0669	0.0573
2.32	0.1479	0.1446	0.1404	0.1347	0.1275	0.1189	0.1126	0.1021	0.0909	0.0794	0.0683	0.0586
2.29	0.1502	0.1469	0.1426	0.1368	0.1295	0.1208	0.1144	0.1038	0.0925	0.0808	0.0696	0.0600
2.26	0.1526	0.1492	0.1449	0.1390	0.1316	0.1228	0.1162	0.1055	0.0941	0.0823	0.0711	0.0615
2.23	0.1550	0.1515	0.1472	0.1412	0.1337	0.1248	0.1181	0.1073	0.0957	0.0838	0.0725	0.0629
2.20	0.1575	0.1539	0.1495	0.1435	0.1358	0.1268	0.1200	0.1090	0.0973	0.0854	0.0740	0.0644
2.17	0.1599	0.1563	0.1519	0.1457	0.1380	0.1288	0.1220	0.1108	0.0990	0.0870	0.0756	0.0660
2.14	0.1624	0.1588	0.1543	0.1480	0.1402	0.1308	0.1239	0.1127	0.1007	0.0886	0.0772	0.0676
2.11	0.1650	0.1613	0.1567	0.1503	0.1424	0.1329	0.1259	0.1145	0.1025	0.0902	0.0788	0.0692
2.08	0.1675	0.1638	0.1591	0.1527	0.1446	0.1351	0.1280	0.1164	0.1042	0.0919	0.0805	0.0709
2.05	0.1701	0.1663	0.1616	0.1551	0.1469	0.1372	0.1300	0.1184	0.1061	0.0937	0.0822	0.0726
2.02	0.1728	0.1689	0.1641	0.1575	0.1492	0.1394	0.1321	0.1203	0.1079	0.0955	0.0839	0.0744
1.99	0.1754	0.1715	0.1667	0.1600	0.1516	0.1416	0.1343	0.1223	0.1098	0.0973	0.0857	0.0762
1.96	0.1782	0.1742	0.1693	0.1625	0.1539	0.1439	0.1364	0.1244	0.1117	0.0991	0.0876	0.0781
1.93	0.1809	0.1769	0.1719	0.1650	0.1563	0.1462	0.1386	0.1264	0.1137	0.1010	0.0895	0.0800
1.90	0.1837	0.1796	0.1745	0.1675	0.1588	0.1485	0.1408	0.1286	0.1157	0.1030	0.0914	0.0819
1.87	0.1865	0.1823	0.1772	0.1701	0.1613	0.1508	0.1431	0.1307	0.1178	0.1050	0.0934	0.0839
1.84	0.1893	0.1851	0.1799	0.1728	0.1638	0.1532	0.1454	0.1329	0.1199	0.1071	0.0955	0.0860

$-\log_{10}\Phi$	Three phase contact angle, $\alpha$ (deg)											
	0	12	18	24	30	36	40	46	52	58	64	70
1.81	0.1922	0.1879	0.1827	0.1754	0.1663	0.1556	0.1478	0.1351	0.1220	0.1092	0.0976	0.0881
1.78	0.1951	0.1908	0.1854	0.1781	0.1689	0.1581	0.1501	0.1374	0.1242	0.1113	0.0997	0.0902
1.75	0.1980	0.1937	0.1883	0.1808	0.1715	0.1606	0.1525	0.1397	0.1264	0.1135	0.1019	0.0925
1.72	0.2010	0.1966	0.1911	0.1836	0.1742	0.1631	0.1550	0.1420	0.1287	0.1158	0.1042	0.0947
1.69	0.2040	0.1995	0.1940	0.1864	0.1768	0.1657	0.1575	0.1444	0.1310	0.1181	0.1065	0.0970
1.66	0.2070	0.2025	0.1969	0.1892	0.1796	0.1683	0.1600	0.1469	0.1334	0.1204	0.1089	0.0994
1.63	0.2101	0.2055	0.1999	0.1921	0.1823	0.1709	0.1626	0.1494	0.1358	0.1228	0.1113	0.1018
1.60	0.2132	0.2086	0.2028	0.1950	0.1851	0.1736	0.1652	0.1519	0.1383	0.1253	0.1138	0.1042
1.57	0.2163	0.2117	0.2059	0.1979	0.1880	0.1763	0.1679	0.1545	0.1408	0.1278	0.1163	0.1068
1.54	0.2195	0.2148	0.2089	0.2009	0.1908	0.1791	0.1706	0.1571	0.1434	0.1304	0.1189	0.1093
1.51	0.2227	0.2179	0.2120	0.2039	0.1937	0.1819	0.1733	0.1598	0.1460	0.1330	0.1215	0.1120
1.48	0.2259	0.2211	0.2151	0.2069	0.1967	0.1848	0.1761	0.1625	0.1487	0.1357	0.1242	0.1146
1.45	0.2292	0.2243	0.2183	0.2100	0.1997	0.1877	0.1789	0.1653	0.1515	0.1385	0.1270	0.1174
1.42	0.2325	0.2276	0.2215	0.2131	0.2027	0.1906	0.1818	0.1681	0.1543	0.1413	0.1298	0.1202
1.39	0.2358	0.2309	0.2247	0.2162	0.2057	0.1936	0.1848	0.1710	0.1571	0.1441	0.1327	0.1230
1.36	0.2392	0.2342	0.2280	0.2194	0.2088	0.1966	0.1877	0.1739	0.1601	0.1471	0.1356	0.1259
1.33	0.2426	0.2376	0.2313	0.2227	0.2120	0.1997	0.1908	0.1769	0.1630	0.1501	0.1386	0.1289
1.30	0.2460	0.2410	0.2346	0.2259	0.2152	0.2028	0.1938	0.1799	0.1661	0.1531	0.1417	0.1319
1.27	0.2495	0.2444	0.2380	0.2292	0.2184	0.2059	0.1970	0.1830	0.1692	0.1562	0.1448	0.1350

$-\log_{10}\Phi$	Three phase contact angle, $\alpha$ (deg)											
	0	12	18	24	30	36	40	46	52	58	64	70
1.24	0.2530	0.2478	0.2414	0.2326	0.2217	0.2091	0.2001	0.1862	0.1723	0.1594	0.1480	0.1381
1.21	0.2565	0.2513	0.2448	0.2359	0.2250	0.2124	0.2034	0.1894	0.1756	0.1627	0.1512	0.1413
1.18	0.2601	0.2549	0.2483	0.2394	0.2283	0.2157	0.2067	0.1927	0.1789	0.1660	0.1545	0.1446
1.15	0.2637	0.2584	0.2518	0.2428	0.2317	0.2191	0.2100	0.1960	0.1822	0.1693	0.1579	0.1479
1.12	0.2673	0.2620	0.2554	0.2463	0.2352	0.2225	0.2134	0.1994	0.1856	0.1728	0.1613	0.1513
1.09	0.2710	0.2656	0.2590	0.2499	0.2387	0.2259	0.2168	0.2028	0.1891	0.1763	0.1648	0.1547
1.06	0.2747	0.2693	0.2626	0.2534	0.2422	0.2294	0.2203	0.2063	0.1926	0.1798	0.1684	0.1582
1.03	0.2784	0.2730	0.2663	0.2571	0.2458	0.2330	0.2239	0.2099	0.1962	0.1835	0.1720	0.1618
1.00	0.2822	0.2767	0.2699	0.2607	0.2494	0.2366	0.2275	0.2136	0.1999	0.1872	0.1757	0.1654